CHAPTER 1

INTRODUCTION

1.1 Background

Titanium dioxide as a photocatalyst in photocatalytic oxidation/reduction reaction offers potentially a facile and cheap method in removing inorganic and organic pollutants from waste water. Theoretically, heterogeneous photocatalysis is a process involves the occurrence of a chemical reaction in the presence of an illuminated semiconductor [1, 2]. The photocatalytic process leads to oxidation-reduction reaction and finally to the overall mineralization of a wide various type of organic pollutants through their interaction with photogenerated holes or electron to produce $OH^{\bullet}$ radicals [3-6]. Titanium dioxide represents one of the most efficient agent in photocatalysis of which TiO_2 particles requires the application of light with energy higher than the titanium dioxide band gap energy (E_g). Titanium dioxide in anatase form (E_g = 3.2 eV) and for rutile (E_g = 3.0 eV), of which the absorption thresholds correspond to 380 and 410 nm for these two titanium dioxide forms, respectively.

Several preparation methods of TiO_2 have been reported in literatures including sol-gel [7, 8], flame synthesis [9], precipitation [10], and hydrothermal methods [11-13]. Modified sol-gel method via hydrolysis and condensation was used to synthesis nano-sized pure TiO_2 and TiO_2 doping [1, 8-15]. Sol-gel preparation has been several advantages such as the homogeneity and a high level of chemical purity. Furthermore, the sol-gel method has been successfully employed in TiO_2

photocatalyst doping with transition metal ions such as V, Fe and Cu for improving the photocatalytic activity under visible irradiation [16-19].

Doping the photocatalyst with transition metal ions into titanium dioxide can enhance photoactivity and shift the absorption spectrum to the visible region. The effect of transition metal ions dopants on the photocatalytic activity is the dynamics of electron-hole recombination and interfacial charge transfer. TiO_2 particles can be simply substitution or interstially doped with different cations. The dopant ions functiona are both hole and electron traps or they can mediate act in interfacial charge transfer. The degree of dispersion of the metal on the particle surface and the homogeneity of the chemical composition of a single particle depend on the preparation methods of doping with leading to different morphological and crystalline properties of this photocatalyst and on the calcination temperature [20, 21].

Many transition metal ions doped TiO_2 has been widely studied, designed, and developed in order to operate effectively under visible light or solar light irradiation. However, pure TiO_2 cannot use in such range of visible light but can be operated in solar light because the ultraviolet band accounts for approximately 3-5% of the total solar energy. Therefore, it is necessary to develop a photocatalytic system that can be utilized under visible and solar light irradiation. Visible light photoactivity has been introduced into TiO_2 by doping with some transition metal ions. The sunlight is used instead of high cost of UV-illumination, where solar irradiations is highly available making photocatalytic process quite attractive and providing a powerful source from sunlight for waste water pollutant elimination [22-24].

The research work presented in this thesis was concerned for improving the procedures in sol-gel synthesis method and while maintaining the advantages of the high surface area and small particle size of TiO_2. Moreover, an enhancement of photoactivity of transition metal ions (V, Fe, and Cu) doped TiO_2 under UVA, solar light, and visible light irradiation. The overall aim of this thesis is the design and optimize transition metal ions (V, Fe, and Cu) doped TiO_2 photocatalysts that is highly photoactive by utilizing the modified sol-gel method for synthesis. The relationship between the physical and chemical properties of the particles and their photocatalytic activities were investigated.

1.2 TiO_2 photocatalyst

1.2.1. Titanium dioxide

Titanium dioxide (TiO_2) is considered as a semiconductor material, commonly known as titania. Although generally used mainly as a pigment or opacifier, TiO_2 can also be applied in photocatalysis. Three polymorphs of titanium dioxide exist: anatase, rutile, and brookite. All structures of anatase, rutile, and brookite consist of TiO_6^{2-} octahedral, which produce the overall structure of TiO_2. In this structure each Ti atom is surrounded by six oxygen neighboring at the corners of a slightly distorted octahedral. The three crystalline structures differ by the distortion of each octahedral and by the assembly patterns of the octahedral chains. Anatase can be regarded as a built up from octahedrals that are connected by their vertices. Rutile, the edges are connected, and both vertices and edges are connected for brookite. Anatase has four edges sharing per octahedron but no corner oxygen sharing. The arrangement of these octahedral gives the overall structure of anatase as shown in Figure 1.1. In rutile, two edges are shared forming a linear chain. The linear chains are joined to each other by sharing of corner oxygen atom, producing the overall rutile structure as shown in

Figure 1.2. Various types of TiO_2 are listed in Table 1 as a representative in photocatalysts. The octahedral linkages in brookite are such that three edges are shared per octahedron. It has been envisioned that the joining together of these distorted TiO_6^{2-} octahedral forms the overall structure of brookite as shown in Figure 2.3 [25, 26].

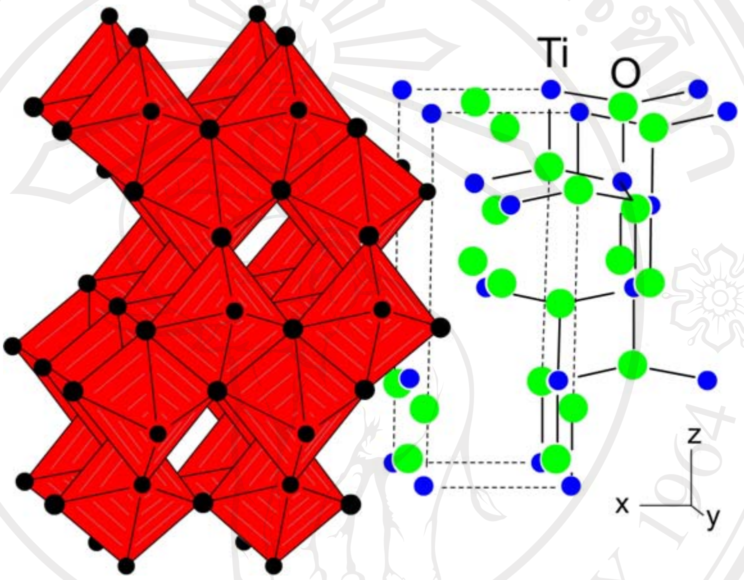

Figure 1.1 The structure of titanium dioxide in anatase phase [25]

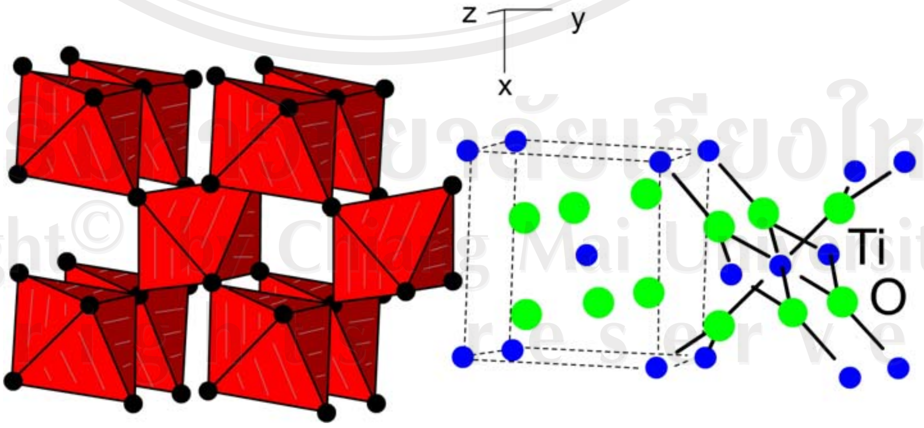

Figure 1.2 The structure of titanium dioxide in rutile phase [25]

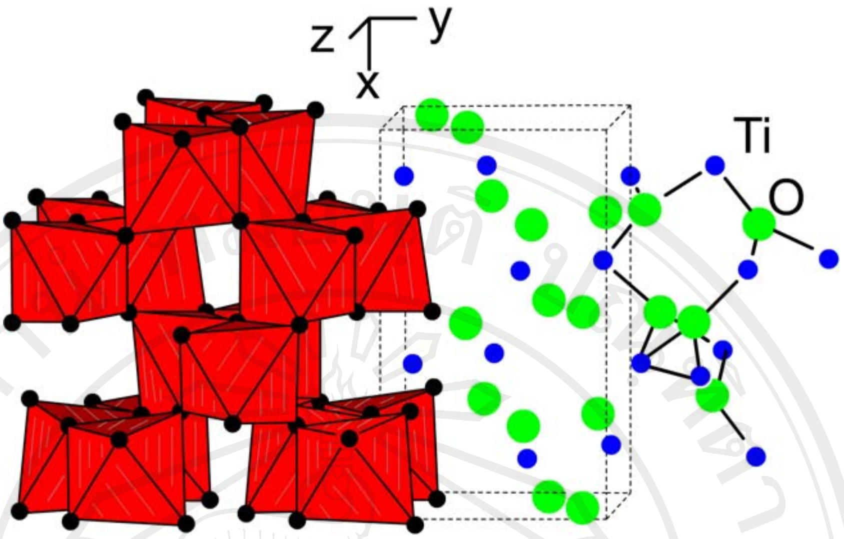

Figure 1.3 The structure of titanium dioxide in brookite phase [25]

Table 1.1 Types and physical properties of titanium dioxide [26, 27]

Properties	**Rutile**	**Anatase**	**Brookite**
Crystalline form	Tetragonal	Tetragonal	Orthorhombic
Atomic weight	79.890	79.890	79.890
Point group	4/mmm	4/mmm	mmm
Space group	$P4_2/mnm$	$I4_1/amd$	Pbca
Density (g/cm^3)	4.27	3.90	4.13
Refractive index	2.72	2.52	2.63
Mohs'hardness	7.0-7.5	5.5-6.0	5.5-6.0
Permittivity	114	48	78
Melting point (°C)	1825	Transformation to rutile	Transformation to rutile

Table 1.2 Chemical and physical properties of titanium [28]

Name	Titanium
Atomic weight	47.90
Density @ 293 K	4.5 g/cm^3
Atomic volume	10.64 cm^3/mol
Boiling point	3558 K
Melting point	1933.2 K
Electronegativity	1.54
Electron affinity	7.6 kJ/mole
Structure	Hexagonal
Atomic radius	147 pm
Ionic radius (Ti^{4+})	0.068 nm
Thermal conductivity	21.9 J/m-sec-deg
Electrical conductivity	23.81 mScm^{-1}

1.2.2 Commercial TiO_2

Degussa P25 was a commercially know of titanium dioxide and was used as a benchmark for comparison though out the studies. The powder of Degussa P25 is composed of anatase 80% and rutile 20% with a specific surface area of 50 m^2/g and is nonporous. The individual particles size is about 30 nm but exists as an aggregate of 200 nm in size [28].

1.3 Properties of transition metal ions

1.3.1 Vanadium [29, 30]

Common oxidation states of vanadium are including +5 to +2 in aqueous solution, as well as the low oxidation states of +1, 0, and -1. Vanadium is the most colorful metal of all the transition elements, showing compounds of every colors and even with considerable color variation within each oxidation state. Vanadium (atomic number 23) occurs in a silver-grey metal having a body-centered cubic crystal structure. The outer electronic configuration in the ground state is $3d^3$ $4s^2$. The maximum oxidation state is thus +5, corresponding to d^0 configuration. Most compounds in this oxidation state are consequently diamagnetic and frequently colorless. The oxidation states including +4, +3, and +2 of compounds are generally having colored and paramagnetic with magnetic moments corresponding to one, two, and three unpaired electrons per vanadium atom.

Vanadium (V) behave in a strongly oxidizing state, its thermally stable compounds are largely limited to those containing the electronegative ligands oxide and fluoride. The oxide V_2O_5 is the most important oxide and most of vanadium chemicals are derived from it. It is a brown poisonous solid obtained from complete oxidation of the metal or its sulfides, nitrides, or lower oxides. It is also formed when vanadium (V) oxohalides are hydrolyzed and when ammonium vanadate is heated.

The +4 oxidation state is the most important one for vanadium in aqueous solutions; it is neither strongly oxidizing nor reducing, and the acidified solutions are stable to atmospheric oxidation. In this oxidation state vanadium has the outer electron configuration $3d^2$ in the ground state. Magnetically dilute vanadium (III) compounds have magnetic moments close to the spin-only value at room temperature. The only important simple compounds of V(III) are the halides, all of which are known, and the oxide is V_2O_3. However, a large number of complexes can be isolated from aqueous as well as nonaqueous solutions. In many respects the chemistry of vanadium (III) closely resembles to titanium (III).

Compounds of vanadium (II) are strong reducing agents and difficult to work with in aqueous solution because of their rapid oxidation. The oxide VO is a basic oxide with the rock-salt structure; it is usually not stoichiometric. It dissolves in acids to give the $[V(H_2O)_6]^{2+}$ ion. This ion is also obtained as the final product in the reduction of NH_4VO_3 by zinc and acid. The chemical and physical properties of vanadium are shown in Table 1.3.

Table 1.3 Chemical and physical properties of vanadium [30]

Name	Vanadium
Atomic weight	50.9415
Density @ 293 K	5.8 g/cm^3
Atomic volume	8.78 cm^3/mol
Boiling point	3623 K
Melting point	2163.2 K
Electronegativity	1.63
Electron affinity	50.7 kJ/mole
Structure	bcc: body centered cubic
Atomic radius	134 pm
Ionic radius (V^{4+})	0.061 nm
Thermal conductivity	30.7 J/m-sec-deg
Electrical conductivity	39.37 mScm^{-1}

1.3.2 Iron [29, 31-32]

Iron is the fourth most abundant element in the earth’s crust; in the elemental form it occurs only but in the combined state and universally common. Iron is the first member of the group VIII triad, lying above ruthenium and osmium. Iron does not show the maximum oxidation state corresponding to the removal of all (eight) of its valence electrons. The maximum oxidation state is +6 but states above +3 are all relatively unimportant; notice that with iron it is the +3 state that has the completely half-filled ($3d^5$) shell. Two structural types of iron occur in the solid state. The α-form, stable at room temperature, has a body-centered cubic lattice. At about 910 °C the α-form is transformed into the γ-form which has a cubic close-packed structure. Iron combines with most nonmetals upon heating. The finely divided metal is pyrophoric in air at room temperature, the massive metal forming ferric oxide (Fe_2O_3) and Fe_3O_4 in air above 150 °C. Steam reacts above 500 °C, forming magnetile (Fe_3O_4) and ferrous oxide (FeO) with liberation of hydrogen. Iron (II) compounds give larger shifts than iron (III) compounds, since the 4s electrons in Fe^{2+} are more strongly screened by the extra 3d electron. The salts of iron nitrate undergo hydrolysis in water with the formation of a brown color; this color disappears if the solution is acidified.

Fe_2O_3 is very affected by a reducing atmosphere where it can act as a flux in both bodies and glazes at high temperatures. Its fluxing action in reduction is quite remarkable and can be demonstrated using a line blend in a clear glaze. Higher amounts of iron exhibit dramatically increased fluidity. Fe_2O_3 is the most natural state of iron oxide where it is combined with the maximum amount of oxygen. In oxidation firing it remains in this form to typically produce amber to yellow up to 4% in glazes (especially with lead and calcium), tans around 6% and browns in greater amounts. In the 20% range, matteness is typical. However, once it reduces to FeO and immediately begins fluxing and forming a glass state, it is difficult to reoxidize. Since the breakdown of carbon or sulfur compounds in body and glaze so easily reduces iron, a slow and very thoroughly oxidizing atmosphere is critical through the 700-900 °C range to assure that all the iron remains in its antiflux oxidized form.

Fe_3O_4 is an intermediate form of iron which is brown in color and exhibits intermediate properties. Fe_3O_4 can either be a mixed of FeO and Fe_2O_3 resulting from an incomplete conversion from one type to the other, or it can be a completely different mineral form of iron known as magnetic iron oxide from the ore magnetite. The latter is a hard crystalline material of use in producing specking in bodies and glazes. The chemical and physical properties of iron are shown in Table 1.4.

Table 1.4 Chemical and physical properties of iron [31, 32]

Name	Iron
Atomic weight	55.847
Density @ 293 K	7.86 g/cm^3
Atomic volume	7.1 cm^3/mol
Boiling point	3023 K
Melting point	1808.2 K
Electronegativity	1.9
Electron affinity	15.7 kJ/mole
Structure	bcc: body-centered cubic
Atomic radius	126 pm
Ionic radius (Fe^{3+})	0.064 nm
Thermal conductivity	72.8 J/m-sec-deg
Electrical conductivity	102.987 mScm^{-1}

1.3.3 Copper [29, 33]

Copper is a soft reddish metal noted for its high thermal and electrical conductivity. The pure metal is used extensively in electrical equipment, as well as in alloys. The metal oxidizes in air at red heat to CuO; at higher temperatures Cu_2O is formed. Copper (III) is isoelectronic with nickel (II) but only a few compounds of copper in this oxidation state have been characterized (no compounds of copper in oxidation states greater than +3 are known). Copper (II) is the most stable state in aqueous solution and it has d^9 configuration. A wide range of stereochemistry is exhibited by copper (II) compounds, with four, five, and six coordination predominating; in each structure variations from idealized geometries occur through bond length and bond angle distortions. The distorted octahedral compounds have magnetic moments in excess of the spin-only-moment. Copper (I) has the closed-shell $3d^{10}$ configuration; its compounds are diamagnetic and colorless (except for those salts having colored anions or in which charge transfer transitions are of low energy). In solid compounds, copper (I) is often the thermodynamically stable state at moderate temperature; for example, CuO and $CuBr_2$ give Cu_2O and CuBr upon heating. The anhydrous copper (II) nitrate exists in two crystalline forms; these have complex structures in which copper ions are linked infinite array by nitrate ions. The nitrate can be sublimed in a vacuum without decomposition. Discrete $Cu(NO_3)_2$ molecules occur in the vapor, in which the copper atoms are four coordinated by oxygen atoms from bidentate nitrate groups. The deep-blue hydrate $Cu(NO_3)_2 \cdot 3H_2O$ crystallizes from aqueous solutions; it is very soluble in water. The chemical and physical properties of copper are shown in Table 1.5.

Table 1.5 Chemical and physical properties of copper [33]

Name	Copper
Atomic weight	63.546
Density @ 293 K	8.96 g/cm^3
Melting point	1356.6 K
Boiling point	2843 K
Electronegativity	1.95
Electron affinity	118.5 kJ/mole
Structure	fcc: face centered cubic
Atomic radius	128 pm
Ionic radius (Cu^{2+})	0.059 nm
Thermal conductivity	401 J/m-sec-deg
Electrical conductivity	595.8 1/mohm-cm

1.4 Heterogeneous photocatalysis [34-39]

1.4.1 Semiconductors as photocatalysts

The heterogeneous photocatalyst has been predicted properties by using band theory. Briefly, the band gap is the range of forbidden energies between non-overlapping bands and the band gap energy characterizes the band structure of a solid. Heterogeneous photocatalysis is a process involves the occurrence of a chemical reaction in the presence of an illuminated semiconductor. A semiconductor can act as a photocatalyst due to its specific electronic structure which is characterized by a filled valence band and an empty conduction band. Figure 1.4 compares the band structure of metal, semiconductors, and insulators. The semiconductors are distinguished by the width of the energy gap. The allowable energies of electrons in a crystal are called the energy levels. In crystal with an atomic lattice, the neighboring nuclei influence the electronic structure and sharp energy levels (e.g. those associated with single atoms) become band of energy, each band representing specific quantum states. Forbidden bands exist between these bands. Electrons giving rise to chemical bonding constitute a valence band as shown in Figure 1.4.

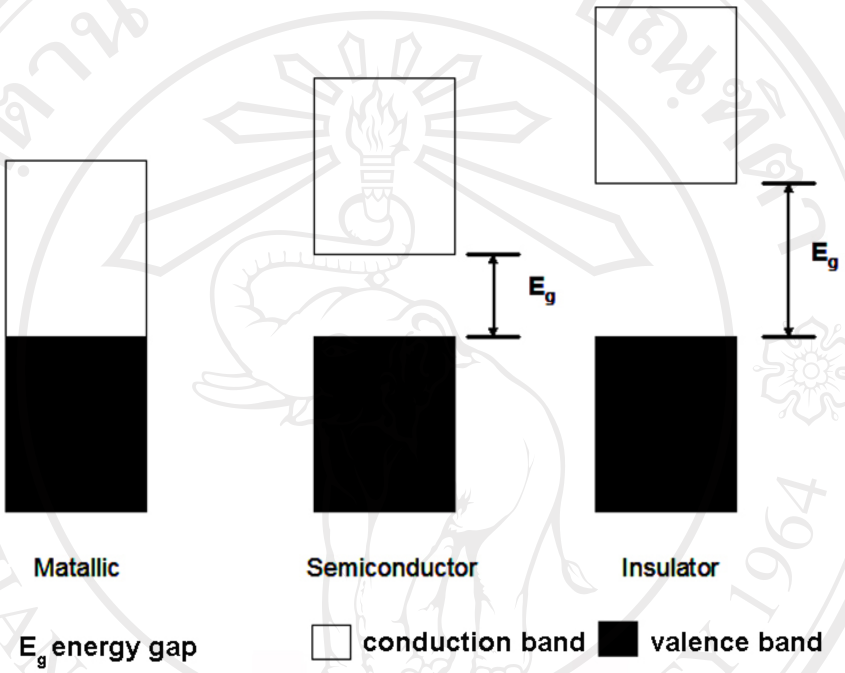

Figure 1.4 Energy band diagrams for metallic, semiconductor, and insulator [38]

The energy gap between valence band and conduction band of metallic solids are connected, therefore atoms are closely packed together. The characteristic properties of metallic conductor are high electrical and thermal conductivity, and high optical reflectivity. In the insulator has a higher band gap, hence the promotion of an electron from the valence band to the conduction band is difficult. The electrical conductivity of semiconductor is ordinarily much smaller than that of a metal due to the limited concentration of free electron and holes. The band gap of a semiconductor lies between a metallic solid and an insulator. Therefore, the promotion of electrons from the valence band to the conduction band, leaving holes in semiconductors, can be achieved easily relative to insulators and subsequently utilized during the photocatalytic process. In particular, TiO_2, with relatively large band gap energy of 3.0 to 3.2 eV as shown in Figure 1.5, can achieve a powerful oxidation-reduction reaction with the ultraviolet rays present in our living environment. It is known that active oxygen and radical species existing in the presence of oxygen and water take part in the oxidation reduction reaction.

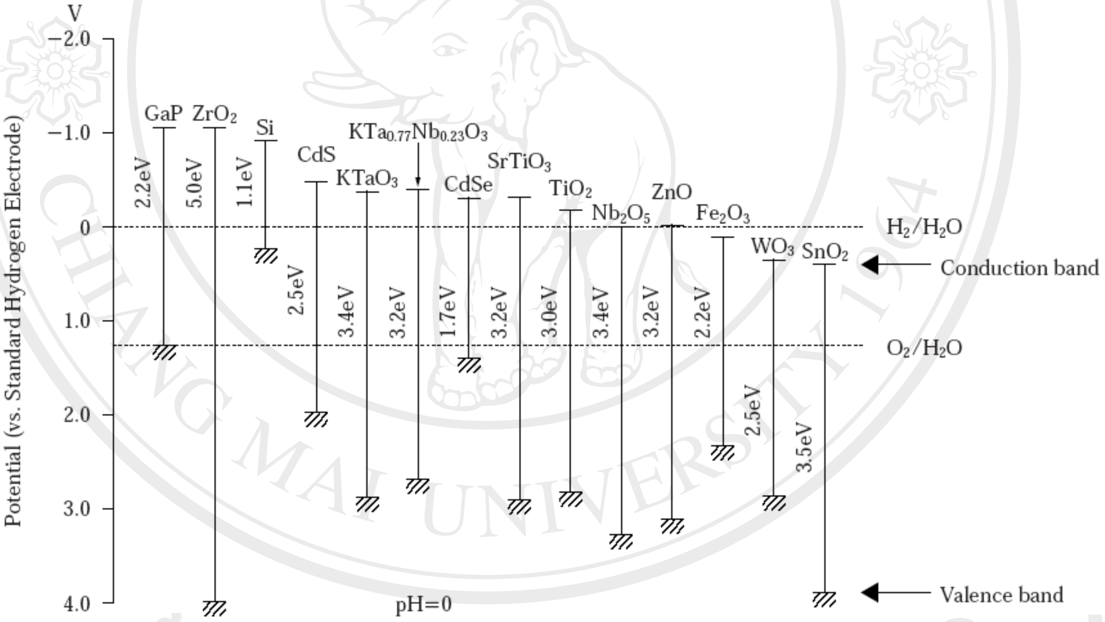

Figure 1.5 Energy structures of various photosemiconductors [39]

1.4.2 Principles of heterogeneous photocatalytic processes

When a solid A, absorbs a photon of light, hν, the result is a molecule in its excited state, A*. This is can be written the following (reaction 1):

$$A+h\nu \rightarrow A^* \qquad (1.1)$$

It is this extra energy in the molecule that allows the photocatalytic reaction to occur. The electronic structure of semiconductors titanium dioxide to act as a sensitizer for light induced redox processes. Figure 1.6 shows a simplified diagram depicting the photoactivation of a semiconductor catalyst. When a semiconductor metal oxide is exposed to light, the photon energy, hν, equal to or more than the band gap, E_g, of the semiconductor is absorbed at its surface. This absorption excites the electron (e^-) resulting in their promotion from the ground state, that is, conduction band, leaving a positive hole (h^+). The holes and electrons produced during the photoexcitation of a semiconductor are referred to as electron-hole pairs and are highly energetic and highly reactive. Figure 1.6 shows the activation of a semiconductor, after excitation with light greater than band gap energy has created an electron-hole pair, the following reactions can occur:

1. reduction of an electron acceptor at the surface by a photogenerated electron,
2. oxidation of an electron donor at the surface by a photogenerated holes,
3. electron-hole recombination in the bulk or at the surface, which generated heat.

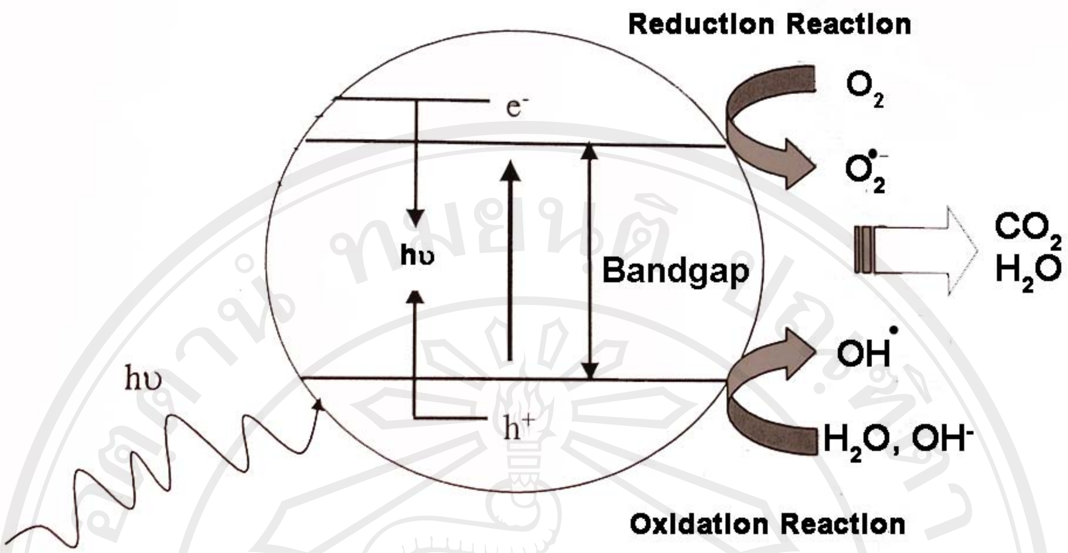

Figure 1.6 Simplified diagram of the mechanism for activation of semiconductor photocatalyst [36].

Heterogeneous photocatalysis can be carried out in various media: gas phase, pure organic liquid phases or aqueous solutions. The classical heterogeneous catalysis, the overall process can be decomposed into five independent steps: [37, 40]

1. Transfer of the reactants in the fluid phase to the surface
2. Adsorption of a least one of the reactants
3. Reaction in the adsorbed phase
4. Desorption of the products
5. Removal of the products from the interface region

The photocatalytic reaction occurs in the adsorbed phase (Step 3). The only difference with conventional catalysis is the mode of activation of the catalyst in which the thermal activation is replaced by a photonic activation as developed.

The activation mode is not concerned with step 1, 2, 4 and 5, although photoadsorption and photodesorption of reactants, mainly oxygen, do exist.

Conduction band electrons (e^-) and valence band holes (h^+) are generated when photocatalyst (TiO_2) particles is irradiated with light energy equal to or greater than the band gap energy. Conduction band electrons and valence band holes migrate to the surface of catalyst where they take part in a series of redox reactions, described by the following reactions below (1.2) to (1.13). Reaction (1.2) represents the formation of the charge carriers upon the illumination of the charge carriers. If these generated charge carriers are not involved in any further reactions, they can quickly recombine. The photogenerated hole can be oxidized either the organic molecule directly, or the OH^- ions and H_2O molecules adsorbed at the TiO_2 surface produce hydroxyl radicals (reaction 1.3 to 1.5). The hydroxyl radicals are the main oxidants for direct degradation of the organic compounds (D: electron donors) (reaction 1.6). The way of the oxidative leads to many case of mineralization of organic substrate to CO_2 and H_2O. The photogenerated electrons react with the dissolved oxygen to form superoxide ions (reaction 1.7). These can also form hydroxyl ions after further reactions (reactions 1.8 to 1.12). The direct reaction between the organic molecules and the holes can also lead to the destruction of the organics (reaction 1.6). The electrons can also directly react with electron acceptors (A) (reaction 1.13) [37, 40].

1. Electron-hole pair generation

$$TiO_2 \rightarrow TiO_2\,(e^-_{cb}, h^+_{vb}) \rightarrow \text{recombination} \tag{1.2}$$

2. Possible traps for holes

(a) Surface adsorbed water molecules

$$TiO_2(h^+_{vb})+H_2O_{ads} \rightarrow TiO_2+OH^\cdot_{ads}+H^+ \tag{1.3}$$

$$TiO_2(h^+_{vb})+H_2O_{ads} \rightarrow TiO_2 +1/2O_2+H^+ \tag{1.4}$$

(b) Surface adsorbed hydroxyl ions

$$TiO_2(h^+_{vb})+OH^-_{ads} \rightarrow TiO_2+ OH^\cdot_{ads} \tag{1.5}$$

(c) Electron donor D species

$$TiO_2(h^+_{vb})+D_{ads} \rightarrow TiO_2+D^+_{ads} \tag{1.6}$$

3. Possible traps for electrons

$$TiO_2(e^-_{cb})+O_{2ads}+H^+ \rightarrow TiO_2+OH^\cdot_2 \leftrightarrow O^{\cdot -}_2+H^+ \tag{1.7}$$

$$OH^\cdot_2+ TiO_2(e^-_{cb})+ H^+ \rightarrow TiO_2+ H_2O \tag{1.8}$$

$$2OH^\cdot_2 \rightarrow H_2O_2+O_2 \tag{1.9}$$

$$H_2O_2+ O^{\cdot -}_2 \rightarrow OH^\cdot+O_2+OH^- \tag{1.10}$$

$$H_2O_2+h\nu \rightarrow 2OH^\cdot \tag{1.11}$$

$$H_2O_2+ TiO_2(e^-_{cb}) \rightarrow TiO_2+OH^\cdot+OH^- \tag{1.12}$$

$$TiO_2(e^-_{vb})+A_{ads} \rightarrow TiO_2+A^+_{ads} \tag{1.13}$$

4. Recombination

$$TiO_2(e^-_{cb}+h^+_{vb}) \rightarrow TiO_2+\text{energy} \tag{1.14}$$

1.4.3 Photocatalytic oxidation

The photooxidation of organic compounds has been interested for many environmental such as waste water pollutant treatments. Many kinds of organic compounds have been reported to be degraded by photocatalytic process. The photooxidation of organic compounds proceeds via hydroxyl radical or directly by the photogenerated holes. Evidence that the hydroxyl radical is the main reactive oxidant in the photocatalytic degradation has been obtained by observing the intermediates of the photooxidation of halogenated aromatic compounds which are the same as those when these compounds were reacted with a known source of hydroxyl radicals [40].

1.4.4 Photocatalytic reduction

Photogenerated electrons at the conduction band of TiO_2 are relatively weaker reductants. However, the presence added electron donor as organic hole scavenger is important in photocatalytic reduction process because it can be enhanced the reaction. In addition, hole scavengers, or some organic compounds could form reducing intermediates upon reacting with the hydroxyl radicals which could enhance the reduction reactions [41].

1.5 Modified photocatalysts: enhancement of photocatalytic activity

Interfacial charge transfer in the reactions when occurs could enhance the photoactivity. Improved charge separation and inhibition of charge carrier recombination is essential in improving the overall quantum efficiency for interfacial charge transfer. This can be achieved by modifying the properties of the particles by a selective surface treatment.

1.5.1 Doping with transition metal ions [42, 43]

The performance of photocatalysts can be changed by doping the transition metal ions into titanium dioxide particles. The dynamics of electron-hole recombination and interfacial charge transfer will be affected. While some studies have shown that doping with transition metal ion into TiO_2 semiconductors can be effective in lengthening the lifetime of the generated charge carriers. Several reasons in the research papers explained the effects of the dopant ions on TiO_2. One reason is that the location and co-ordination of the dopant ions within the semiconductor. This depends critically on the sample preparation techniques, pretreatment, and the concentration of the dopant ions. The dopant ions may be adsorbed on the surface, or incorporated into the interior of the particle upon firing, or they may form separate oxide phases. The dopant ions can function as both hole and electron trap or they can mediate interfacial charge transfer. Once incorporated into the interior of TiO_2, the dopant ions may occupy either lattice substitutional or interstitial sites. Their ability to function as trap site and/or to mediate interfacial charge transfer will depend on these factors. Finally, the site where the electron gets trap greatly influences the redox chemistry of the doped semiconductor. However, if an electron is trapped in a deep trapping site, it will have a longer lifetime, but it may also have a lower redox potential. This might result in a decrease in the photoreactivity.

1.5.2 Metal ion deposition [39, 41, 42, 44]

Metal ion deposition onto titanium dioxide and its effects on photocatalytic reactions have been studied extensively. Metal ions deposition, mostly noble metals due to noble metal can enhance the reaction of photocatalysis, on the surface of the photocatalyst is also utilized enhance the separation of electron-hole pairs. When metal ion deposition on semiconductor, it can change the semiconductor surface properties. Figure 1.7 illustrates the metal ion in contact with surface of semiconductor. Upon excitation, electron can migrate to the metal deposit where they can be trapped or captured by an oxidant (A^+-electron acceptor). The hole is then free to migrate to the surface where oxidation can be occur (D (electron donor) $\rightarrow D^+$).

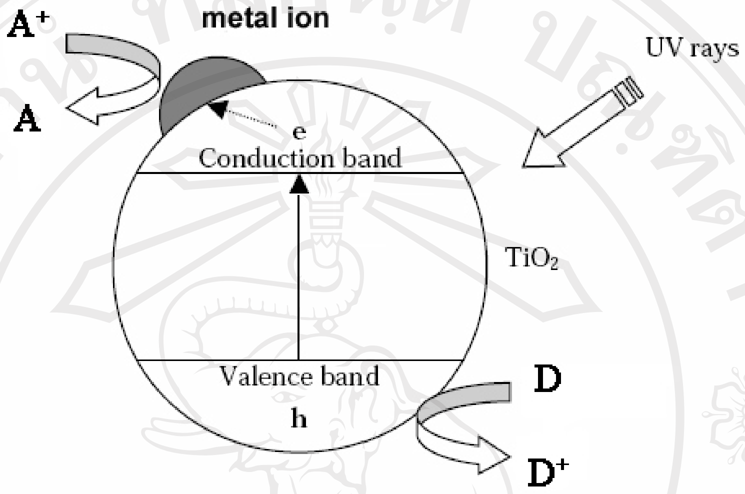

Figure 1.7 Electron mediation by metal ion in contact with TiO_2 surface [39]

The ability of a metal to mediate the photogenerated electrons away from the semiconductor may give rise to a schottky barrier. A schottky barrier is created at a metal-semiconductor interface. The potential barrier formed at the interface depends on the work functions of the two materials. The work function (Φ) is defined as the energy difference between the vacuum level E_{vac} and the Fermi level E_F. The vacuum level E_{vac} is defined as the energy of an electron at rest (and hence with zero kinetic energy) just outside the crystal surface and not interacting with the crystal. When the metal and semiconductor are brought into intimate contact, electron flow from the semiconductor to the metal until the Fermi level on both side are equalized. The transfer of electrons could be rationalized as follows: the energy barrier for the electron transfer from a region of higher work function (metal ions) to one of lower work function semiconductor (TiO_2) is greater than that from a lower work function to one the higher work function [42].

1.5.3 Coupled semiconductors [1, 42, 44, 45]

In a coupled semiconductor system the two particles are in contact with each other and both holes and electrons are accessible on the surface for selective oxidation and reduction processes. The possessing different energy levels for their corresponding conduction and valence bands, provides an approach to achieve a more efficient charge separation, an increased lifetime of the charge carriers and an enhanced interfacial charge transfer to adsorbed substrates. An interesting approach to prevent electron-hole recombination is the coupling of two semiconductor catalyst to improve charge separation. This strategy accomplishes vector displacement of charges on the semiconductors and reduces electron-hole recombination. Thus, coupled semiconductor systems offer potential advantages for solar energy utilization because of the possibilities presented by inter-particle electron transfer.

1.5.4 Application of nano-sized particles [46]

Nano-sized of particle to a certain “critical size” produces the so-called quantum size effects (Q-size). Quantum-size effects occur when the particles size of the semiconductor smaller than Bohr radius of the first excitation state. One of the most detached effects of reducing the size of a particle to that of quantum size is increase band gap energy. The band gap energy can be increased because as the particle size approaches that of nano-sized, the photogenerated electron and hole cannot fit into such as a particle unless they assume a state of higher kinetic energy. There seem to be many discrepancies in the reported quantum size of TiO_2 particle possibly due to the different crystalline phases of the particles. However, it can be taken that crystalline TiO_2 starts to show Q-size effect at about 10 nm. Q-size effects could be obvious by the absorption shift to shorter wavelength or also known as blue-shift.

1.6 Factor influencing photocatalytic activity [37, 47, 48]

Several chemical and physical parameters have been shown to affect the photocatalytic process. Many factors can be influence with photocatalytic activity such as extrinsic parameters and intrinsic parameters. Extrinsic parameters are external factors such as pH of the solution, the initial concentration of the organic compound, the light intensity, the catalyst dosage, and the temperature. The intrinsic parameters are internal factor of photocatalyst such as the crystallographic phase, the inter-atomic spacing and the crystallite size of the catalytic material.

1.6.1. Extrinsic parameters

1.6.1.1 Light intensity

Generally, organic compound can be degraded by using TiO_2 under UV light illumination but under visible light it can not degrade the organic compound. Therefore, light intensity has influence the photocatalytic activity. It has also been shown that an excess of light promotes a faster electron-hole recombination [49].

1.6.1.2 Temperature

Herrmann (1999) [37] reported that the effect of temperature on the photocatalytic activity at the temperature ranging from 20 °C to 80 °C was not significant. This is because a photocatalyst is activated by the absorption of photon, and hence its true activation energy (E_t) is nil whereas its apparent activation energy (E_a) is often very low in this temperature range. At very low temperature such as

< 0 °C, activities decrease and E_a becomes positive. This is attributed to the low temperature favoring adsorption, which is a spontaneous exothermic phenomenon. Hence, the intermediates and the final products formed could be strongly adsorbed, impeding the adsorption of the substrates to be degraded and hence decreasing the photocatalytic activity. At temperature grater than 80 °C, the exothermic adsorption process is suppressed and the adsorption of substrates becomes difficult. Under these conditions, the activity decreases and E_a tends to be negative [37, 50, 51].

1.6.1.3 Photocatalyst loading [37]

The rate of chemical reaction initially increases with an increase in the catalyst loading, as this translates into an increase in the number of available active sites. The catalyst loading is an important factor in which the number of active sites depened on optimum loading. It has been found that the optimal catalyst dosage is dependent on the light intensity as well. The higher the light intensity is, the higher the optimal catalyst loading.

1.6.1.4 Influence of pH [52, 53]

The pH of the solution has significant influences on the photocatalytic degradation process. The effect of pH on the reaction rate can be interpreted in terms of electrostatic interactions between charged TiO_2 particles and the contaminants. This in turn affects adsorption processes, since photocatalytic reactions are believed to be surface reactions. A variation in pH also affects the surface due to the amphoteric nature of titanium dioxide particles.

1.6.2 Intrinsic parameters

1.6.2.1 Effect of surface area on photoactivity

High surface area is considered an advantage in terms of a greater concentration of active sites per square meter, and hence leading to higher reactivity. However, it has often been reported that while the activity of the TiO_2 catalyst is affected by its external surface, photocatalytic activity is not a function of the surface area alone [54-56].

1.6.2.2 Effect of particle size on photoactivity [57-59]

The effect of particle size on the photocatalytic activity can be interpreted in terms of its effect on the surface area which can be explained in terms of an increase in the number of active sites per square meter, as well a greater adsorption ability of the pollutants on the catalyst surface.

1.6.2.3 The importance of the crystal structure [60, 61]

Anatase phase is normally employed to degrade the organic compounds which due to its higher active sites than rutile and brookite phases. Some researchers reports have proposed that the high degree of hydroxylation is one of the most important characteristic for anatase phase when compared with rutile phase.

1.7 Application for titanium dioxide [39, 62, 63]

1.7.1 Self-sterilizing photocatalytic

TiO_2 can be coated on tile surface, walls, ceiling, and floor which its detrimental effect on bacteria and viruses. They decomposed on the surface of coating due to the strong oxidizing properties of TiO_2. The covered walls, ceiling and floor with photocatalytic TiO_2 tiles, even bacteria floating in the air such as in an operating room are also killed as they come in contact with this surface.

1.7.2 Self-cleaning photocatalytic of building materials for indoor and outdoor application

Titanium dioxide can be coated on so many types of building materials. These coats exhibit a self-cleaning effect due to the strongly oxidizing properties as well as the superhydrophilic properties. Moreover, TiO_2 can be coated on glass lamp on highway tunnel lighting fixtures which normally darken from the automobile exhaust. When titanium dioxide-coated lamp covers are used, the glass surface remains cleaner and last longer, and the number of required cleanings is greatly reduced.

1.7.3 Anti-fogging glass

Generally, if moist air comes in contact with glass, small water droplets form, and the glass becomes fogged. On TiO_2-coated glass, the water forms a continuous flat sheet, so that there is no fogging. This is example of what we call "superhydrophilicity" in previous subsection (1.7.2).

1.7.4 Photocatalytic water purification

World-wide environmental crisis is growing daily and in intensity. Expectations are high for the environment-cleaning capability of titanium dioxide photocatalyst (Listed in Table 1.6. are some possible applications). Water treatment is divided into various subclasses, such as the treatment of drinking water, sewage water, industrial wastewater, agricultural discharge water, and water in the swimming pools and in storage tanks.

Table 1.6 Environmental applications of TiO_2 photocatalysis [64]

Possible environmental application of TiO_2 photocatalysis		
Field	**Objects**	**Required function**
Water	- distribution system for potable water - lakes/dams water storage tanks - ports/bays - semiconductor factory drainage - golf course drainage	- toxic materials/odor elimination - aquatic herbicide /disinfection/ adsorption - aquatic herbicide/disinfection/cleanup - crude oil spill breakdown - chloroethylene breakdown - pesticide breakdown
	- NO_x disposal - interior living area - hospitals	- oxidation - odor elimination - disinfection
soil	- playground sandboxes - livestock area - golf courses	- disinfection - odor elimination - herbicide

1.8 Preparation of photocatalysts

The selection in preparation of catalysts methods are important in order to produce the best catalyst. Even though the relationship between formation procedures and ultimate catalyst behavior may in many cases be obscure, an understanding of some of the effects produced with typical catalyst ingredients by manipulations such as precipitation, washing, drying, and heating are claimed to be an art rather than science.

1.8.1 Sol-gel method

The sol-gel technique is a two-reaction process consists of hydrolysis and condensation. Two types of precursor route are known: the non-alkoxide and the alkoxide route. The non-alkoxide route for sol-gel preparation employs inorganic salts such as nitrates, chlorides, acetates, carbonates, acetylacetonates, etc. After sol-gel reaction, non alkoxide route is requires an additional removal of the inorganic anion. Second technique, is by using the alkoxide route as a starting material for sol-gel preparing. The sol-gel process involves the formation of a TiO_2 sol or gel or precipitation by hydrolysis and condensation reaction of titanium alkoxide. Condensation reaction is included oxolation and olation, which then transformed into an oxide network. The olation step could leave the alcohol molecule which is coming from a protonated alkoxy ligands and water molecule coming from a solvated alkoxide. The condensation by oxolation of alkoxide could transform to alkoxy ligand and to hydroxo ligand and eventually to form the oxo. The reaction schemes were described by Reaction (1.15)-(1.18). Particles of titanium hydroxides produced from sol-gel route in aqueous medium generally possesses electrical charge due to the amphoteric dissociation of surface hydroxyl groups and the adsorption of H^+/OH^- [1, 66].

1. Hydrolysis

$$M(OR)_n + H_2O \rightarrow M(OR)_{n-1}(OH) + ROH \tag{1.15}$$

2. Condensation

Oxolation:

$$M(OR)_n + M(OR)_{n-1}(OH) \rightarrow M_2O(OR)_{2n-2} + ROH \tag{1.16}$$

Olation:

$$2M(OR)_{n-1}(OH) \rightarrow M_2O(OR)_{2n-2} + H_2O \tag{1.17}$$

Overall reaction:

$$M(OR)_n + n/2H_2O \rightarrow MO_{n/2} + nROH \tag{1.18}$$

The sol-gel method is required heat treatment to remove the organic part and to separate the crystalline either anatase or rutile phase of TiO_2. Sol-gel method is successfully synthesized nanoparticles using low temperature less than which is 100 °C and possessed high surface area [1, 66-69]. The calcination process will certainly cause a loss of surface hydroxyl groups, decline in surface area, and even induce phase transformation. The washing step is considered to be the important factor and also has been reported for causing surface modifications. Cleaning of particles is usually achieved by washing the surface with a solvent followed by centrifugation. The solvent can affect the chemical composition and crystallization. The particle washing could affect the surface charge of the particles by bonding onto the surface. The sol-gel method has many advantages over other fabrication technique for high purity and homogeneity of powder. Sol-gel methods coupled with hydrothermal routes for mesoporous structures lead to large surface area. Moreover, metal ions-doped TiO_2 can be synthesized by sol-gel method for use as a photocatalyst under UVA, solar light, and visible light irradiation [70-72].

1.8.2 Precipitation method [1, 73-76]

The precipitation method of TiO_2 is prepared by the addition of basic solution (NaOH, NH_4OH, urea) to a raw material and followed by calcination to crystallize of titanium dioxide. The disadvantage is the control of particle size and size distribution, in fast (uncontrolled) precipitation often causes the formation of larger particles instead of nano-sized particles.

1.8.3 Solvothermal method [1, 77-79]

This method employs chemical reactions in aqueous (hydrothermal method) or organic media (solvothermal method) such as methanol, 1,4 butanol, toluene under self-produced pressures at relatively low temperatures (usually under 250 °C). The solvothermal method could be beneficial to control particle size, particle morphology, and crystalline phase. Moreover, the surface chemistry properties can be control by using the solution composition, reaction temperature, pressure, solvent properties, additives, and ageing time.

1.8.4 Microemulsion method [1, 80-81]

Synthesis of nanoparticles has been successfully utilized water in oil microemulsion. Microemulsion may be defined as thermodynamically stable, optically isotopic solution of two immiscible liquids consisting of microdomains of one or both stabilized by an interfacial film of surfactant. The surfactant molecule generally has a polar (hydrophilic) head and a long-chained aliphatic (hydrophobic) tail. Such molecules optimize their interactions by residing at the two-liquid interface, thereby considerably reducing the interfacial tension.

1.8.5 Combustion synthesis [1, 82-83]

Combustion synthesis leads to highly crystalline fine and has large area particles. The synthetic process involves a rapid heating of a solution/compound containing redox mixtures/redox groups. During combustion, the temperature the reaches high point of temperature for a short period of time (1–2 min) making the nanoparticles material.

1.8.6 Impregnation method [84, 85]

Impregnation method is the simple method of making a catalyst. The powder of catalyst is contacted with a solution then dried and calcined. The impregnation technique requires less equipment since the filtering and forming steps are eliminated and washing may not be needed. It is the preferred method in preparing metal ions coating on surface of semiconductors such as TiO_2, ZnO, and SnO_2 due to its simplicity.

1.8.7 Hydrothermal method [86-89]

Hydrothermal method is a prospective method to obtain nanocrystalline TiO_2 particles, where mophology, particle size and crystallinity could be controlled by many conditions such as precursor route, pH, and temperature. Nevertheless, it is required a low temperature for materials development, widely applied in industrial processes for ceramic synthesis. The hydrothermal technique is required an autoclave instrumentation and relies on the extensive heating of the particles diluted in an aqueous solution or slurry over a long period of time. Fine-tuning of the semiconducting nanoparticle size and specific active area critically affects the desired properties of the photocatalysts by varying the surface to volume ratio, by affecting the photo excited charge transfer and by influencing the surface hydroxyl concentration crystallinity. Hydrothermal method can also be used to change the morphology and phase composition of materials by varying the reaction parameters. However, it has been difficult to achieve a large surface area and high crystallinity simultaneously such as in the case of nonporous TiO_2 by carrying out hydrothermal treatment.

1.9 Characterization techniques

1.9.1 X-ray diffraction method [26, 40, 85]

X-ray diffraction (XRD) is now a standard method for characterization of catalyst and generally has been employed to determine the crystalline phases, including solid solutions, and to measure the particles size and shape. It is also possible to follow *in situ* XRD changes that occur during activation and testing of catalysts.

Monochromatic X-ray, incident on a crystalline solid, is diffracted owing to the crystal structure of the solid. For a maximum to occur in the diffraction pattern at a particular angle of incidence θ (with respect to lattice planes (hkl), the Bragg equation must be followed

$$n\lambda = 2d_{\mathrm{hkl}} \sin\theta_{\mathrm{hkl}} \tag{1.19}$$

where:

d_{hkl} = interplanar distance between (*hkl*) planes,

n = order of diffraction,

λ = wavelength of incident X-rays (e.g. 1.542 Å for copper K_α X-rays).

1.9.1.1 Identification of phases by XRD

XRD data is normally used for the phase identification, whereby the XRD pattern of a sample being examined can be compared with a Joint Committee Powder Diffraction Standards (JCPDS file no.).

1.9.1.2 Particle size measurement by XRD [26, 40, 85]

For good quality crystalline material of dimension 0.1 nm is made up of approximately 1,000,000 crystal planes (assuming that $d_{\mathrm{hkl}} = 1$ nm). When an X-ray collides with these planes close to the Bragg angle, diffraction intensity is not observed because the X-rays reflected from the multitude of parallel planes annihilate one another. With such materials diffraction peaks are produced only within a very narrow window very close to the Bragg angle. Particle sizes are often in the range 1-100 nm for heterogeneous catalysts. In such circumstances the number of stacked planes per particle is in the range of 5-100. This results in the broadening of the XRD peaks because there are insufficient reflecting planes to annihilate phase reflection at angle that are fairly far removed from the Bragg angle.

This effect has been quantified as the Scherrer equation:

$$t_{\mathrm{hkl}} = K\lambda / B_{\mathrm{hkl}} \cos\theta_{\mathrm{hkl}} \qquad (1.20)$$

where:

t_{hkl} is the particle size measured from X-rays diffracted from the (*hkl*) planes,

B is the peak width measured at half height measured in radius,

θ is the Bragg angle for the reflection, and

K is a constant which depends to some extent on the particles shape. For spherical particles $K = 0.9$.

Scheme 1.8 demonstrates how particle size and shape can be determined by XRD analysis. A sample was analyzed by XRD and exhibited the pattern shown, namely one very narrow line and one rather broad one. In this case the apparent conflict is caused by the shape of particle. X-rays reflected from the (100) planes 'see' a large particle and a narrow line results. X-rays reflected from the (001) planes 'see' a small particle and a broad line results.

When measuring particles size using XRD line broadening it is important to realize that the not all the broadening is due to the particle size effect. Near perfect crystals should produce extremely narrow XRD lines, but even here some broadening occurs because of instrumental factors. Instrumental contribution to line broadening is subtracted out by running the XRD of a good quality polycrystalline sample of the same materials.

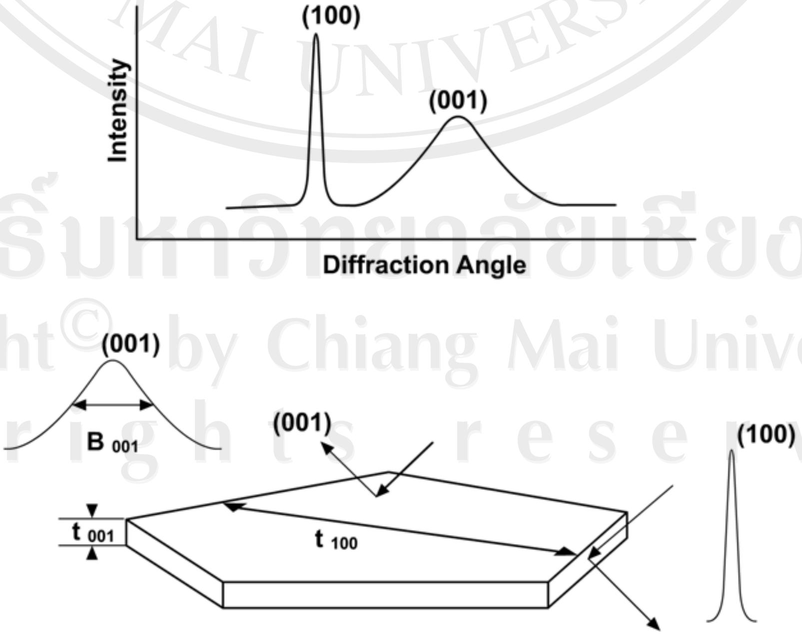

Figure 1.8 Schematic diagram of X-ray line broadening effects [40]

1.9.2 Surface area and porosity determination [26, 40, 85]

1.9.2.1 Surface area determination

Brunauer, Emmett and Teller developed the now famous BET equation for the determination of the surface area of a solid. The method is base on non-specific physisorption of a gas (N_2 or Ar) onto a solid close to the condensation temperature of the adsorbing gas. Adsorption is characterized by an isotherm which represents the equilibrium amount of gas adsorbed on a solid at a given temperature as a function of pressure. Figure 1.9 is a typical II isotherm which forms the basis of the BET analysis. This figure shows formation of a near monolayer of adsorbate at low pressures, followed by multilayer formation which accelerates at high partial pressures. Hysteresis is observed also at p/p_0 above 0.8, namely differing behavior for whether the isotherm is determined by progressive addition or removal of adsorbate gas to the system.

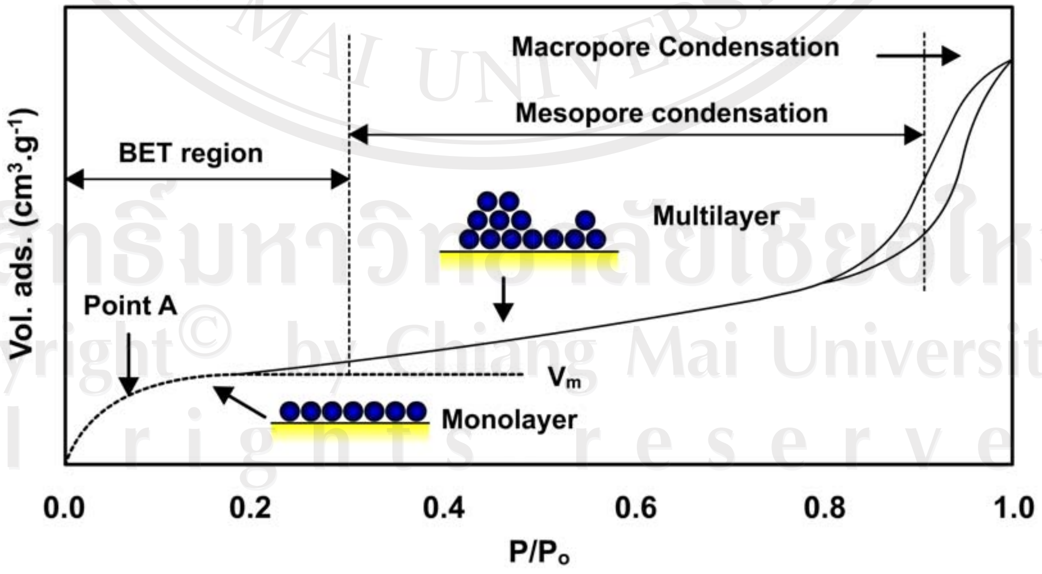

Figure 1.9 Typical isotherm for N_2 adsorption-desorption on γ-Al_2O_3 [40]

Point A in Figure 1.9 corresponds to the stage at which there is approximately monolayer coverage. There is a difficulty in determining this point exactly as multilayer physisorption which can occur before monolayer coverage is complete. BET equation is as follow:

$$\frac{p}{V(p_0 - p)} = \frac{1}{V_m C} + \frac{(C-1)p}{C V_m p_0} \tag{1.21}$$

where:

V is the volume, reduced to standard conditions (STP) of gas adsorbed per unit mass of adsorbent at a given pressure, p and constant temperature,

p_0 is the saturation pressure at the measurement temperature,

V_m is the volume of gas adsorbed at STP per unit mass of adsorbent, when the surface is covered by a unimolecule layer of adsorbate, and

C is a constant, related to the free energy of adsorption.

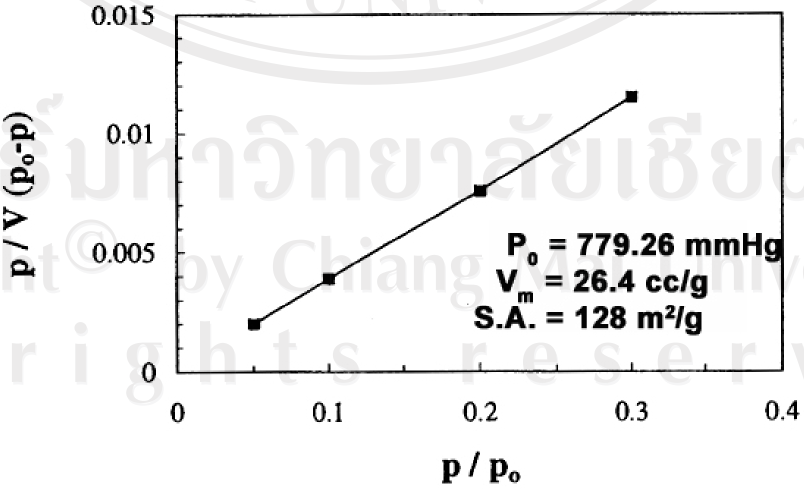

Figure 1.10 BET plot for surface area (S.A.) determination for γ-Al_2O_3 [40]

According to equation 1.21 a plot of $p/V(p_0-p)$ versus p/p_0 should yield a straight line. The surface area is then calculated using:

$$S_{\mathrm{BET}} = \frac{V_{\mathrm{m}} A_{\mathrm{m}} N_{\mathrm{a}}}{V_{\mathrm{mol}}} \qquad (1.22)$$

where:

N_{a} is Avogadro's number (6.02×10^{23}),

V_{mol} is the molar volume of absorbate gas at STP (22.4 mol^{-1}),

A_{m} is the cross-sectional area of absorbed gas ($A_m(N_2) = 0.162\ \mathrm{nm}^2$).

When nitrogen is the adsorbing gas this reduces to:

$$S_{\mathrm{BET}} = 4.353 V_{\mathrm{m}} \qquad (1.23)$$

The BET equation is applicable within the range of relative pressures $0.05 < p/p_0 < 0.3$. At higher relative pressures, the BET equation is usually inaccurate owing to the effects of capillary condensation in the smallest micropores. Figure 1.10 shows analysis of the data from Figure 1.9 in the range $0 < p/p_0 < 0.3$. The surface area in this case was 128 m^2/g.

1.9.2.2 Pore size distribution [40]

The International Union of Pure and Applied Chemistry (IUPAC) have classified pores into several size ranges. Pores with diameters less than 2 nm are termed micropores, pores with a diameter greater then 2 nm but less than 50 nm are termed 'transitional' or mesopores, while pores with diameters greater than 50 nm are terms macropores. In addition to the determination of the surface area of porous solids it is essential that the pore shape and pore size distributions are know to describe completely the textural properties of porous solids.

Traditionally pores with diameters less than 50 nm have been determined by nitrogen adsorption-desorption isotherms, while pores diameters greater than 100 nm have been measured with mercury porosimeters.

Two separate approaches are required to determine micropore and mesopore size distributions. For micropores devised a method for the determination of micropore area distribution and micropore volume distributions (the MP method) by manipulation of isotherm adsorption data Figure 1.11. It is essentially a modification of Lippens and de Boer's, *t*-method where the variation of the thickness (*t*) of adsorbed N_2 layers with relative pressure (p/p_0) on a porous solid is compared with a standard *t*-curve from a non-porous solid. The thickness of the adsorbed N_2 layers is obtained by dividing the liquid volume of N_2 adsorbed by BET surface area:

$$t = \frac{V_{\mathrm{liq}}}{S_{\mathrm{BET}}} \times 10^3 \ (\mathrm{nm}) \qquad (1.24)$$

At higher relative pressures (higher values of t) deviations from a straight line due to micropore capillary condensation are used to evaluate micropore shape, size and volume distributions.

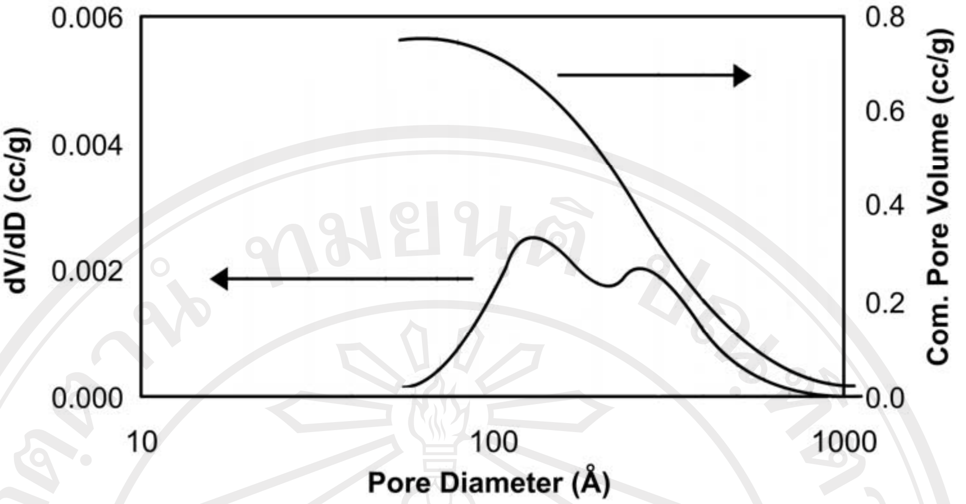

Figure 1.11 BJH analysis of data from Figure 1.10 showing differential and cumulative mesopore volume distributions for γ-Al_2O_3 [40]

Information on mesopores comes from the isotherm at p/p_0 values above 0.25. The isotherm is Figure 1.9 shows a splitting into an adsorption and a desorption branch. This hysteresis contains valuable information on mesopore geometry and the phenomenon is governed by the Kelvin equation. The Kelvin equation with N_2 as the adsorbate is:

$$r_k = \frac{0.415}{\log(p_0/p)} \qquad (1.25)$$

The Kelvin radius (r_k) indicates that radius into which condensation occurs at the required relative pressure. The actual pore radius is given by:

$$r_p = r_k + t \tag{1.26}$$

The term t refers to thickness of a multilayer of adsorbed N_2 existing on the pore wall when evaporation or condensation occurs which is of the same depth as the adsorbed N_2 layer on a non porous surface.

$$t = 3.54\left[\frac{5}{2.303\log(p/p_0)}\right]^{1/2} \tag{1.27}$$

Numerical integration methods such as the BJH method can be used to evaluate mesopore area and volume distribution utilizing the Halsey equation. Figure 1.11 presents a BJH treatment of the isotherm shown in Figure 1.9, in terms of cumulative mesopore volume and size distribution.

1.9.3 Transmission electron microscopy and diffraction [26, 40, 90]

Electron microscopy (EM) provides local structure information about the samples in both real and reciprocal space, for example local structural information about the surface and the bulk of the sample at the atomic level, together with chemical, electronic and three-dimensional structural information are now routinely available. Electron-sample interactions and scattering are fundamental to EM. EM is a diffraction technique in which crystals diffract electrons in accordance with Bragg's law, $n\lambda = 2d\sin\theta$, where λ is the wavelength of the electrons, d is the lattice planar spacing of the hkl reflection and θ is the scattering angle. Discovery of the electron and the particles and wave duality of electrons has been well documented in the literature. The electron has a low mass and is negatively charged. It can be easily deflected when close to electron and the positive nucleus of the sample atom. These interactions are termed Coulombic or electrostatic interactions and lead to electron scattering. Electron microscopy deals with a complex electron wave with both its amplitude and phase modulated, as the electrons interact with matter. This interaction generates elastic scattering and a variety of other signals which can be used to obtain structural and chemical information about a sample as shown in Figure 1.12(a). Elastic scattering occurs when incident electrons interact with the potential field formed by the nuclei of matter involved with essentially no energy loss in momentum transfer, whilst inelastic scattering occurs when interactions between incident electrons and the electrons of matter occur and scattered electrons lose energy.

Transmission electron microscope (TEM), electrons are transmitted through the sample. Normally the incident and scattered electrons are referred to as electron beams. In TEM, the electron beam is transmitted through the instrument's optics. The TEM has an electron gun and electromagnetic lenses which include condenser and objective lenses. The condenser lenses converge and control the electron beam and illuminate the sample, and the objective lenses forms the image of the sample and diffraction. The images and diffractions are then magnified by other lenses in the system. A base reference line passing through the centre of all the lenses is called the optic axis of the electron microscope.

Figure 1.12(*b*) shows a 'ray diagram' for a finite object which scatters radiation and can be used to understand the image formation in an electron microscope. Rays scattered at an angle θ are gathered by the objective lens and converged to a point in the image plane. Parallel rays are focused in the back focal plane (bfp) of the lens. The intensity distribution in the bfp gives rise to diffraction.

The diffraction pattern formed may be regarded as the Fourier Transform (FT) of the crystal. An apertured inverse Fourier transforms (FT) in the objective lens forms the image. The objective lens takes the electrons emerging from the exit surface of the sample and disperses them to create an electron diffraction pattern (DP) in the bfp and recombines them to form an image in the image plan. In a TEM, accelerating electron voltages are normally between 100-400 keV and lower (a few hundred electron volts to ~30 keV) for scanning EM (SEM). Principles of EM imaging and diffraction are shown in Figure 1.12(*c*). In EM, a two-dimensional planar projection of a three-dimensional object is observed.

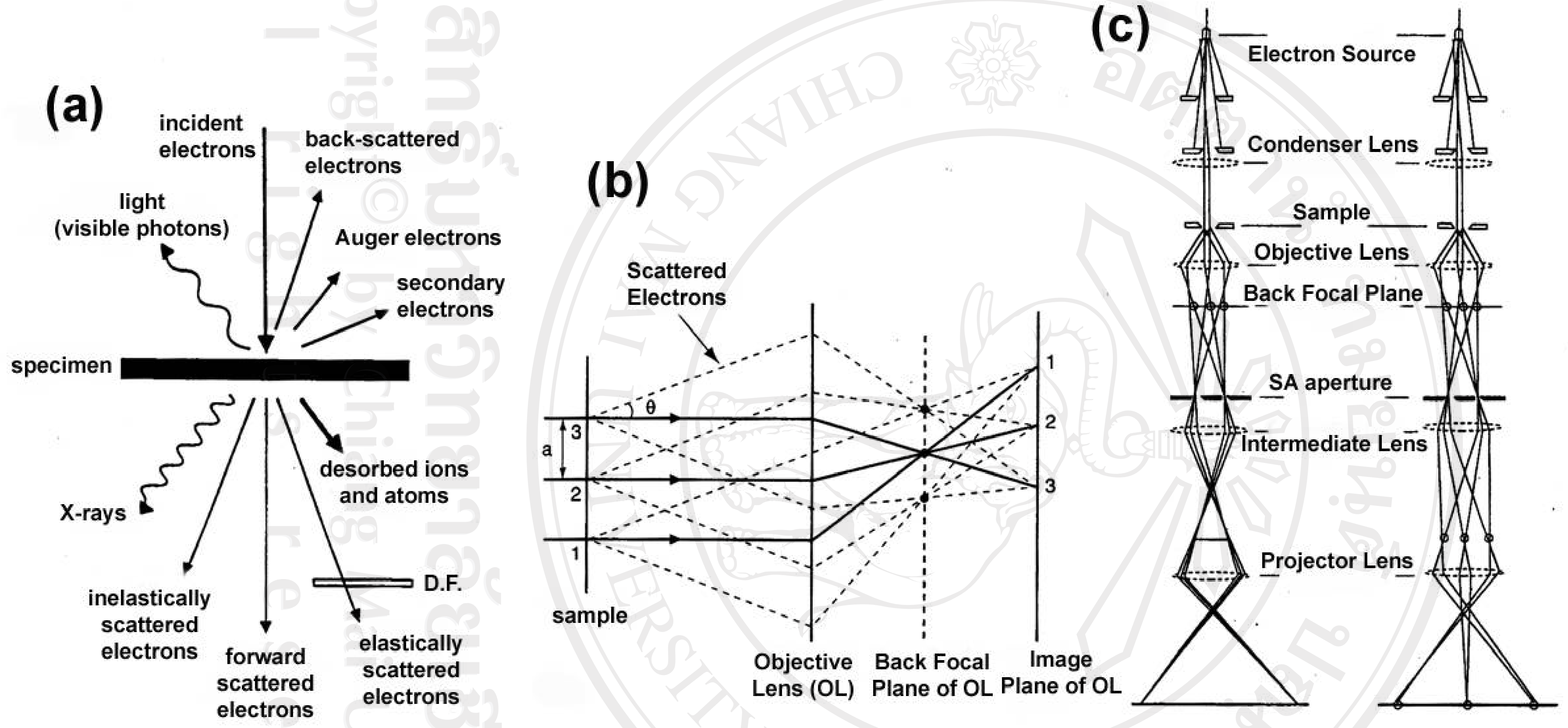

Figure 1.12 (a) Signals generated during electron beam-sample interactions; (b) a 'ray diagram' of image formation; and (c) a schematic diagram of the principles of electron microscopy: (A) imaging and (B) diffraction [26].

1.9.4 Chemical composition analysis [26, 40, 90]

Analytical EM using electron-stimulated characteristic X-rays is a well-known chemical composition characterization technique for analyzing materials. High spatial resolution chemical analyses (from areas of a few nm or less) using electron nanoprobes are now possible in a modern EM and can provide information of the catalyst composition at the subnanometer level. Details of EDX in the EM are described and some important definitions are highlighted in the following sections.

1.9.4.1 X-ray spectroscopy in the electron microscope [90]

In electron-sample interactions, X-rays can be formed during inelastic scattering of electrons. The following principles describe the generation and character of the X-rays.

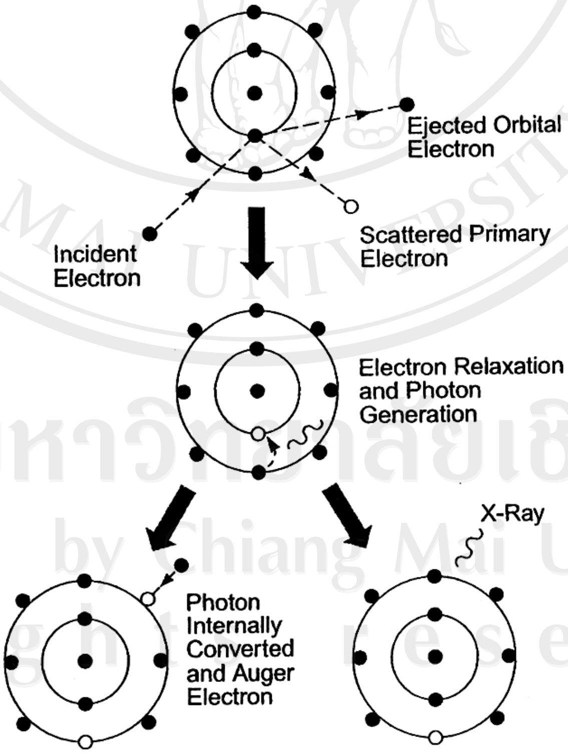

Figure 1.13 The process of electron-stimulated X-ray emission in the electron microscope [26]

Characteristic is described as the interaction between a high-energy electron forms the beam and an inner-shell electron from the sample atom results in the ejection of a bound inner-shell electron from the attractive field of the nucleus in the sample atom, leaving the atom in an excited state with an electron shell vacancy. Deexcitation by transition from the outer shell involves a change in the energy state of the atom between sharply defined levels, producing X-rays (or Auger electrons). The process is elucidated in Figure 1.13. These X-rays are characteristic of the elements in the sample and are used for composition analysis. EDX, in which X-ray intensities are measured as a function of the X-ray energy, is the most convenient and common method for chemical composition analysis in the electron microscope

Continuum is described as the deceleration of beam electrons (i.e. those which do not participate in removing sample electrons) leads to the production of a continuous range of X-rays. They contribute to the background of a spectrum and are termed Bremmsstrahlung X-rays.

Chemical composition analysis complementing the microstructural information obtained from EM is known as analytical EM (AEM). Important compositional variations or non-stoichiometry in a material which is seemingly 'phase pure or stoichiometric' by the criterion of bulk diffraction techniques and compositions of surface layers can be revealed using AEM. For quantitative microanalysis a ratio method for thin crystals is used, given by the equation:

$$C_{\mathrm{A}} / C_{\mathrm{B}} = K_{\mathrm{AB}} I_{\mathrm{A}} / I_{\mathrm{B}} \tag{1.28}$$

where C_A and C_B are the concentrations of elements A and B and I_A and I_B are the background subtracted peak intensities for A and B; and typically a few dozen crystals are analyzed. The sensitivity factor K_{AB} is determined using appropriate standards. For bulk materials, more complex correction procedures are required for atomic number (Z), absorption (A) and X-ray fluorescence (F). Thus, AEM provides real space imaging together with crystallographic and microcompositional information about the sample on the very fine scale. Furthermore, AEM can be used to obtain partial occupancies within cation sites, (and under special conditions, in anion sites). When elemental peaks overlap, wavelength dispersive X-ray spectroscopy (WDS - where X-ray intensities are measured as a function of wavelength) may be advantageous for composition analysis. Detection sensitivity in WDS can be very high (<100 ppm), due to the much higher X-ray count rates.

1.9.4.2 Selected-area diffraction [90]

The technique relies upon the fact that the electron beam after diffraction by the specimen forms a miniature diffraction pattern (ring or spots) in the back focus plane of the objective lens (Figure 1.14(a)). Electron diffracted in the same directions OA, O′A′ come together to form a spot P in the back focal plane of the lens. Similarly the diffraction spot Q is formed by electron diffracted at an equal angle on the opposite side of the undeviated beam. If the first projector lens (or the diffraction lens in a four-lens imaging system) is now weakened so that it is focused in this plane instead of the image plane of the objective lens (i.e. the first intermediate image plane), the pattern is projected and enlarged on to the screen of the microscope. If the lens currents for this mode of imaging are preset the microscope can be switched alternately between imaging the specimen and projecting its diffraction pattern (Figure 1.14(b)).

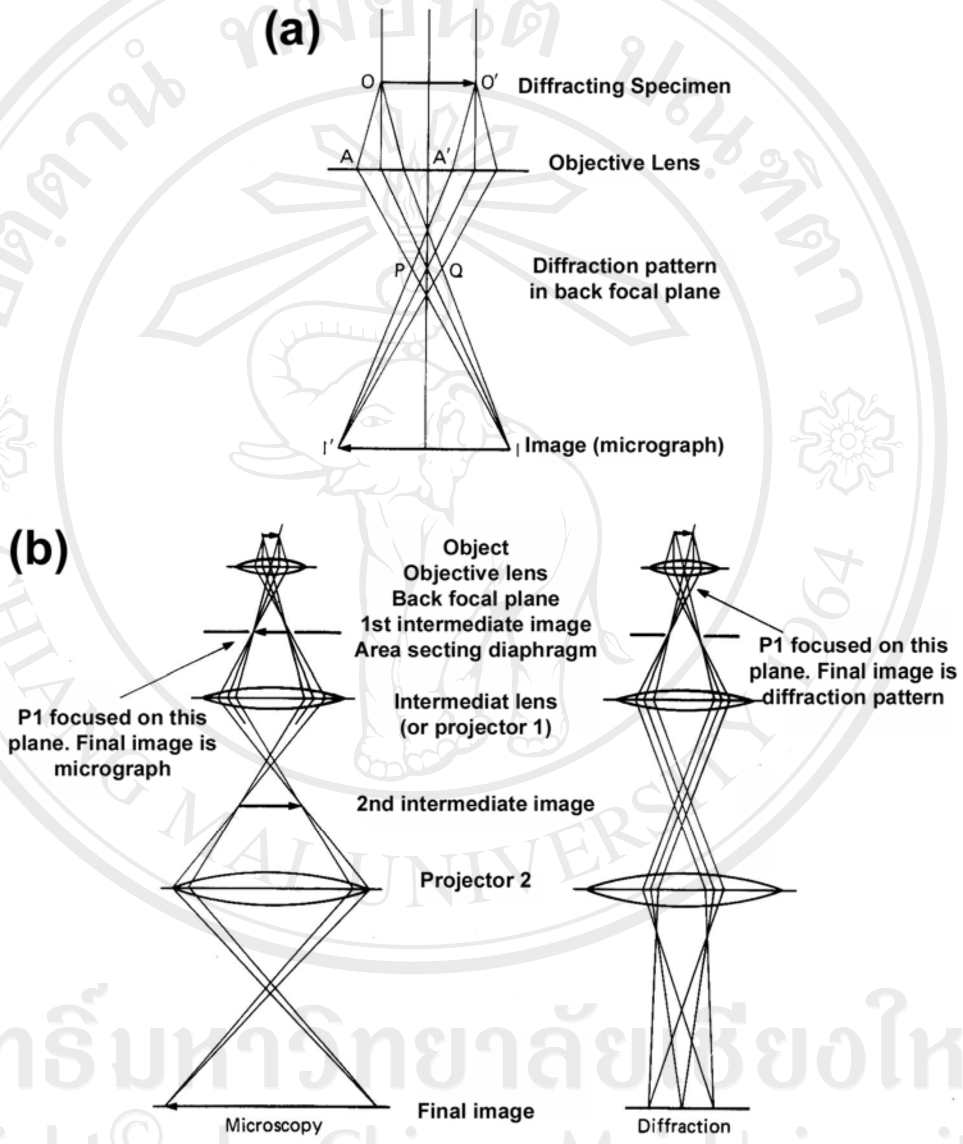

Figure 1.14 (a) Ray diagram showing the formation of the diffraction pattern and intermidate image by the objective lens. (b) In a three-lens microscope the intermediate lens (or projector 1) is normally focused on the intermediate image formed by objective lens [90].

When P1 is weakened to focus on the back focal plane of the objective lens the final image is an enlarged diffraction patterns. The selected area diaphragm ensures that only electrons coming from a chosen region in the specimen contribute to the diffraction pattern. Moreover, if a diaphragm containing an aperture of diameter *D* is inserted into the plane of the first intermediate image it will pass only those electrons coming from a part of the object of diameter *D/M*, where *M* is the magnification of the objective lens. With this area-selecting aperture in place, switching to the diffraction mode results in a diffraction pattern being formed only by those electrons originating from the chosen small area of object.

1.9.4.3 Measurements of electron diffraction patterns [90]

The electron diffraction camera or its equivalent, diffraction stage of the TEM, the relationship $\lambda L = Rd$ can be obtained for the precise determinations of lattice spacing once L has been measured and λ calculated. If the gun voltage is not known accurately it is better to determine the product λL (camera constant) experimentally by calibrating with a stand substance such as thallium chloride or aluminum. Lattice spacing may be measured to 1% by very careful working, but 5% is a more practical aim which may still be sufficiently precise to enable materials to be identified by electron diffraction, using the crystallographic data provided by Joint Committee Powder Diffraction Standards (JCPDS) powder diffraction file. Selected area diffraction can also be very useful for the purely qualitative assessment of the degree of crystallinity of a specimen.

1.9.5 Scanning Electron Microscope (SEM) [91]

Scanning electron microscope, the surface of a solid sample is scanned in a raster pattern with a beam of energetic electrons. Several types of signals are produced from a surface in this process, including backscattered, secondary, and Auger electrons; X-ray fluorescence photons; and other photons of various energies. All of these signals have been used for surface studies, but the two most common are 1) backscattered and secondary electrons, which serve as the basis of scanning electron microscopy, and 2) X-ray emission, which is used in electron microprobe analysis.

1.9.5.1 Instrumentation

Figure 1.15 is a schematic of a combined instrument that is both a scanning electron microscope and a scanning electron microprobe. The common electron gun source and electron focusing system is used but that the electron microscope employs an electron detector, whereas the microprobe uses an X-ray detector. The magnetic condenser and objective lens system shown in Figure 1.15 serve to reduce the image to a final spot size on the sample of 5 to 200 nm. The condenser lens system, which may consist of one or more lenses, is responsible for the through put of the electron beam reaching the objective lens; the objective lens is responsible for the size of the electron beam impinging on the surface of the sample. Typically, an individual lens is cylindrically symmetrical and between 10 and 15 cm in height. Scanning with a SEM is accomplished by the two pairs of electromagnetic coils located within the objective lens (see Figure 1.15); one pair deflects the beam in the x direction across the sample, and the other pair deflects it in the y direction. Scanning is controlled by applying an electrical signal to one pair of scan coils, such that the electron beam strikes the sample to one side of the center axis of the lens system. By varying the electrical signal to this pair of coils as a function of time, the electron beam is moved in a straight line across the sample and then returned to its original position. After completion of the line scan, the other set of coils is used to deflect the beam slightly, and the deflection of the beam using the coils is repeated. Thus, by rapidly moving the beam, the entire sample surface can be irradiated with the electron beam. The signals to the scan coils can be either analog or digital. Digital scanning has the advantage that it offers very reproducible movement and location of the electron beam. The signal from the sample can be encoded and stored in digital form along with digital representations of the x and y positions of the beam. The signals that are used to drive the electron beam in the x and y directions are also used to drive the horizontal and vertical scans of a cathode-ray tube (CRT). The image of the sample is produced by using the output of a detector to control the intensity of the spot on the CRT. This method of scanning produced a map of the sample in which there is a one-to-one correlation between the signal produced at a particular location on the sample surface and a corresponding point on the CRT display. The magnification (M) achievable in the SEM image is given by

$$M=W/w \tag{1.29}$$

where W is the width of the CRT display and w is the width of a single line scan across the sample. Because W is a constant, increased magnification is achieved by decreasing w. The inverse relationship between magnification and the width of the scan across the sample implies that a beam of electrons that has been focused to an in finely small point could provide infinite magnification. A variety of other factors, however, limit the magnification that is achievable to a range from about $10\times$ to $100{,}000\times$.

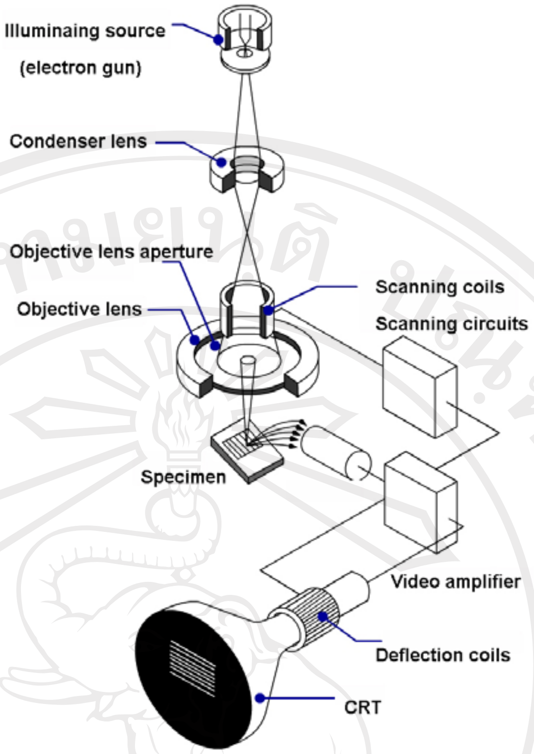

Figure 1.15 Schematic diagram of scanning electron microscope with CRT display [91].

1.9.5.2 Interaction of electron beams with solids

The versatility of the scanning electron microscope and microprobe for the study of solids arises from the wide variety of signals that are generated when the electron beam interacts with the solid. The signals are included: backscattered electrons, secondary electrons, and X-ray emission. The interactions of a solid with an electron beam can be divided into two categories: elastic interactions, which affect the trajectories of the electrons in the beam without altering their energies significantly, and inelastic interactions, which result in transfer of part or all of the energy of the electrons to the solid. The excited solid then emits secondary electrons, Auger electrons, X-rays, and sometimes longer wavelength photons.

- Elastic scattering

When an electron collides elastically with an atom, the direction of the electron changes, but the speed of the electron is virtually unaffected, so that the kinetic energy of the electron remains essentially constant. The angle of deflection for any given collision is random and vary from 0 to 180 deg. Some of the electrons eventually lose energy by inelastic collisions and remain in the solid; the majority, however, undergoes numerous collisions and as a result eventually exits from the surface as backscattered electrons. It is important to note that the beam of backscattered electrons has a much large diameter than the incident beam- that is, for a 5-nm incident beam; the backscattered beam may have a diameter of several micrometers. The diameter of the backscattered beam is one of the factors limiting the resolution of an electron microscope.

- Secondary electron production

The surface of a solid is bombarded with an electron beam having an energy of several keV that electrons having energies of 50 keV or less are emitted from the surface along with the backscattered electrons. The number of these secondary electrons is generally one half to one fifth or less of the number of backscattered electrons. Secondary electrons are produced as a result of interactions between the energetic beam electrons and weakly bound conduction electrons in the solid, which leads to ejection of the conduction band electrons with a few electron volts of energy. Secondary electrons are produced from a depth of only 50 to 500 A° and exit in a beam that is slightly larger in diameter than the incident beam.

- X-ray emission

A third product of electron bombardment of a solid is X-ray photons. Both characteristic line spectra and an X-ray continuum are produced and emitted from the surface of the sample. This radiation serves as a basis for the electron microprobe.

1.9.6 X-ray photoelectron spectroscopy (XPS) [85, 92]

X-ray photoelectron spectroscopy determination of chemical and physical changes of catalysts upon exposure to gaseous molecules and upon different thermal treatments can be examined. XPS specimen is irradiated by a source of essentially monochromatic X-rays under ultrahigh-vacuum conditions. These cause photoionization producing photoelectrons whose kinetic energy is primarily characteristic of X-ray energy and the electron binding energy. The photoelectron kinetic energy, E_k, which is the measured quantity in the experiment, is given by Einstein's law

$$E_k = h\nu - E_b \qquad (1.30)$$

where hν is the energy of the incident radiation and E_b the binding energy of the electron in a particular level.

When the incident photon has enough energetic in many different levels in the sample be ionized and a spectrum is produced and displaying all accessible energy levels as a distribution of photoelectrons with kinetic energies governed by Equation 1.30. Photoelectron peaks are then labeled according to the quantum numbers of the level from which the electron originates. The electron is characterized by a total momentum number $j = l + s$, where l is the orbital momentum number and s

the spin momentum number which is equal to 1/2 or −1/2. Therefore, whenever $l > 0$, the peak is split into a doublet, with an energy difference called *spin-orbit splitting* which increases with Z roughly as $Z5$. The intensity ratio of the two components is determined by the ratio of the multiplicity $(2j + l)$ of the corresponding levels. Additional peaks due to the so called electron *shake-up* process sometimes appear on the high binding energy side of a photoelectron peak. These features correspond to photoelectrons emitted from an atom in which a second electron in a given orbital goes into an excited state as consequence of the sudden change in the atom central potential produced by the photoelectron ejection. In the presence of these types of peaks could be quite useful for chemical state determinations. As a consequence of the primary ionization process, a hole in the core level is created and the excited ion tends to relax by photoemission or by emission of electrons through the Auger decay. The latter is the favorite mechanism for core levels with binding energies below 2 keV. The Auger effect is a multiple ionization process in which an electron from an external level fills the vacancy created in the core level and the difference between the two energy levels is carried away by the ejected Auger electron. The final state is therefore a doubly ionized state with two vacancies in the levels involved in the process. The notation used for the identification of Auger peaks considers all the levels involved in the process. For example, an Auger process referred as KL_2L_3 arises from an ionization of the core electron of the 1s (K) level followed by a contemporary filling of the hole by an electron from the $2p_{1/2}$ (L_2) level and the emission of an electron from the level $2p_{3/2}$ (L_3) or vice versa. The energy of the Auger transition is described by:

$$E_{KL2L3} = E_K - E_{L2} - E_{L3} - F(L_2L_3; X) + R(L_2L_3) \qquad (1.31)$$

where E indicates the binding energies of the involved levels, $F(L_2L_3; X)$ the Coulombic interaction energy between the two holes in the final state, X, and $R(L_2L_3)$ is a relaxation term referring to the collapse of the passive electron orbitals in the doubly ionized state. In Equation 1.31, the kinetic energy of the Auger electrons is related only to the binding energies of the three levels involved in the transition and is independent on the incident energy. Therefore, Auger peaks can be distinguished from photoelectron peaks by changing the excitation photon energy which affects only the position of the photoelectron peaks. Both binding energies and Auger energies give information on the chemical environment of the emitting atom. The XPS technique yields quantitative and qualitative information. Quantitative information arises from the element specificity of the binding energies and the relation between the intensity of the photoelectron peaks and the element concentration. Qualitative information is obtained from the energy position of a photoelectron peak with respect to the energy position of the same level in a reference compound (chemical shift). One of the most important applications of XPS is the determination of the oxidation state of elements at the surface. The electronic binding energy for inner-shell electrons shift as a result of changes in the chemical environment. The exact binding energy of an electron essentially depends upon (i) the level from which photoemission is occurring, (ii) the oxidation state of the atom, (iii) the local chemical environment.

1.9.7 UV-Vis diffuse reflectance spectroscopy (UV-Vis DRS) [34]

In transmission spectroscopy, where a beam of light is passed through a sample, the transmittance is the ratio of intensities of transmitted to incident light:

$$T = \frac{I}{I_0} \tag{1.32}$$

where T is the transmittance (1 for a completely transparent sample), I is the intensity of transmittance light, I_0 the intensity of the incident beam. In an analogous fashion the remittance of a diffusely reflecting sample is the ratio of intensities of reflected to incident light:

$$R_\infty = \frac{J}{I_0} \tag{1.33}$$

where R_∞ is the absolute remittance, J is the intensity of the reflected radiation, and I_0 is again the intensity of the incident beam. The ∞ subscript denotes that the sample is "infinely thick"; in other word, none of the light irradiating the sample penetrates to the bottom of the sample holder. This is usually the case when the sample thickness is approximately 5 mm or more. A perfect diffusely reflecting substance, practically never attained, would have $R_\infty = 1$.

Since it is not practical to measure R_∞, the absorbed remittance, the measured quantity is usually the relative remittance, R'_∞:

$$R_{\infty}^{/} = \frac{R_{\infty\text{sample}}}{R_{\infty\text{standard}}} \qquad (1.34)$$

Notice that if $R_{\infty\text{standard}}=1$, then the absolute and relative remittances must be equal.

The relative remittance is analogous to transmittance in transmission spectroscopy. Transmission spectroscopy is often conveniently present data in absorbance in linear fashion which related to the concentration of absorbing species. In an analogous fashion, it is possible to plot log ($1/R'_{\infty}$) against wavelength or frequency. This is so called apparent absorbance units. This does not imply, however, that Beer's law is valid for diffuse reflectance spectroscopy.

Ideally one would like a function, like Beer's law in transmission spectroscopy, to linearly relate analyst concentration with the reflectance characteristics of a diffusely reflecting sample. The function often use is that derived by Kubelka-Munk:

$$F(R_{\infty}) = \frac{(1-R_{\infty})^2}{2R_{\infty}} = \frac{K}{S} = \frac{2.303\varepsilon C}{S} \qquad (1.35)$$

where K is the absorption coefficient (twice the Beer's law absorption coefficient), S is twice the scattering coefficient of the sample, ε is the absorptivity, and C is the analyst concentration.

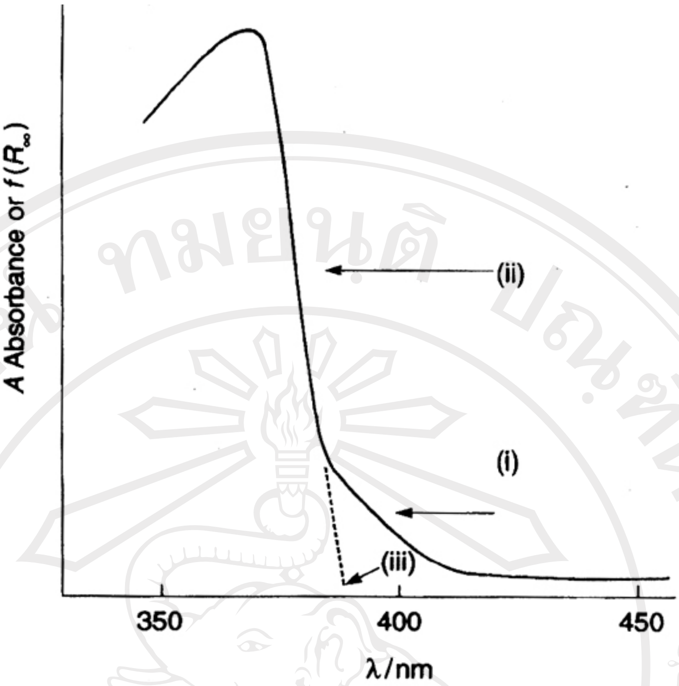

Figure 1.16 Diffuse reflectance spectrum of the fundamental absorption edge of titanium dioxide powder. Absorbance $((F(R_\infty))$ vs. wavelength: (i) indirect transition; (ii) direct transition; (iii) direct band gap; $E_g = hc/\lambda_g$ [34]

The interaction of near-UV photons with a typical photocatalytic material (e.g., finely divided titanium dioxide powder) is illustrated in Figure 1.16. The shape of the absorption edge reveals to some extent the shapes of the densities of electronic states in the valence band and in the adjacent conduction band and a diagrammatic representation of this situation is illustrated in Figure 1.17(a). The onset of the absorption edge (lowest energy) indicates the minimum energy required to effect the excitation of an electron from the highest occupied energy state of the valence band into the lowest available energy state of the conduction band. This transition may not necessarily involve the coupling of the electric vector of the photon directly. The wave functions of the two state involved in the cases where this occurring this process is termed a direct transition and results in a small change ($\Delta\tilde{k} \approx 0$) in the wave vector of the electron involved following its excitation to the conduction band. More frequently, the magnitude of the wave vector ($\tilde{k}'_{cb}$) of the lowest energy state in the conduction band does not correspond to that of the electron at the highest energy of the valence band ($\tilde{k}_{vb}$), and as a consequence of the significant difference in these wave vector ($\Delta\tilde{k}$) requires that the excitation of the electron from the lower state (valence band (vb)) to the highest state (conduction band (cb)) is accompanied by the participation, simultaneously, of an elastic wave within the lattice of the solid (illustrated in Figure 1.17b).

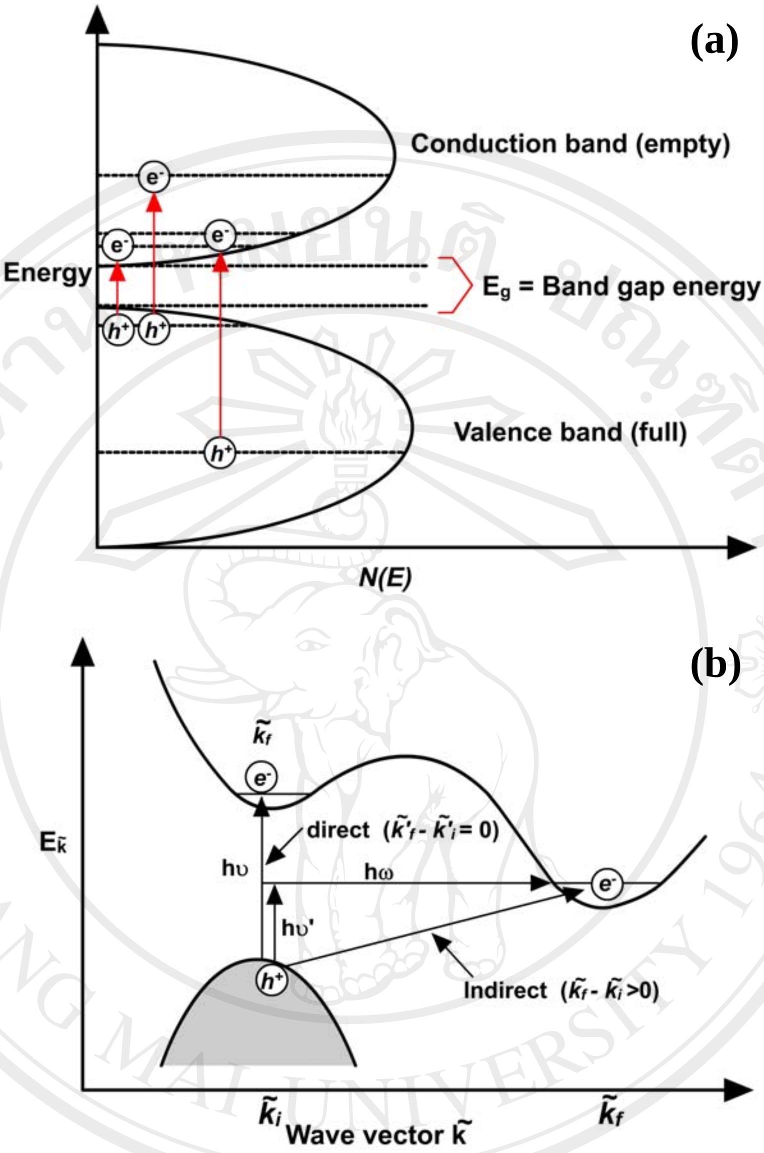

Figure 1.17 (a) Schematic energy band diagram showing hole-electron pair formation as a consequence of differing energies of incident radiation; (b) schematic energy band diagram (energy vs. wave vector $\tilde{k}$) illustrating the difference between direct and indirect transitions [34].

In such circumstances the transition probabilities of the two processes differ significantly in magnitude, a useful analog being with two-body (direct) and three described, the ‘bodies’ are the photon and the electrons in the direct transition or the photon, the phonon and the electron in the indirect transition.

At photon energies higher in magnitude than the minimum required value effect the transitions of the types described. Electrons from the highest occupied states in the valence band can be promoted to a higher energy states within the conduction band or into other unoccupied bands that may exist at even larger energies. In general, the range of energies (ΔE) of the conduction band from its lowest value to the highest will be greater than the corresponding range of energies of the valence band. The onset of absorption may be due to an indirect process with a correspondingly smaller value of $-\mathrm{d}A/\mathrm{d}\lambda$. Direct processes with larger $-\mathrm{d}A/\mathrm{d}\lambda$ values will be likely at higher photon energies. Additionally the adsorption of higher-energy photons may raise electrons from lower-energy states in the valence band to the lower regions of the conduction band. However, the accompanying hole state in the valence band will have a larger momentum than one created nearer to the top of the band.

1.9.8 Fourier transform infrared spectrophotometry (FT-IR) [42, 93, 94]

The region of infrared radiation ordinarily extends from about 2.5 to 16 microns (1 micron = 1 micrometer = 10^{-6} meter). Infrared spectroscopy involves examination of the stretching vibrations. Stretching vibrations change distances between adjacent atoms. Bending vibrations (including scissoring, rocking, twisting, wagging) change bond angles. FT-IR is most useful for identifying chemicals that are either organic or inorganic. It can be utilized to quantify some components of an unknown mixture. It can be applied to the analysis of solids, liquids, and gasses. The term Fourier Transform Infrared Spectroscopy (FT-IR) refers to a fairly recent development in the manner in which the data is collected and converted from an interference pattern to a spectrum. FT-IR instruments are computerized which makes them faster and more sensitive than the older dispersive instruments.

1.9.8.1 Qualitative analysis

FT-IR can be utilized to identify chemicals from spills, paints, polymers, coatings, drugs, and contaminants. FT-IR is perhaps the most powerful tool for identifying types of chemical bonds (functional groups). On absorption of photon of infrared radiation, a molecule is excited to a higher energy level in which vibration motions are more energetic. To some extent, vibration motions involved of part of molecule. Some vibrations are relatively localized, involving mainly two or, at most, a few atoms. Such characteristic absorptions make infrared spectra useful to providing structural information about compounds of unknown structure. By interpreting the infrared absorption spectrum, the chemical bonds in a molecule can be determined. FT-IR spectra of pure compounds are generally so unique that they are like a molecular "fingerprint". While organic compounds have very rich, more detailed spectra than inorganic compounds which are much simpler. For most common materials, the spectrum of an unknown can be identified by a comparison to a library of known compounds.

1.9.8.2 Quantitative analysis

The strength of the absorption is proportional to the concentration. FT-IR can be used for some quantitative analyses. Usually these are rather simple types of tests in the concentration range of a few ppm up to the percent level.

1.9.8.3 Physical principles

Molecular bonds vibrate at various frequencies depending on the elements and the type of bonds. For any given bond, there are several specific frequencies at which it can vibrate. According to quantum mechanics, these frequencies correspond to the ground state (lowest frequency) and several excited states (higher frequencies). One way to cause the frequency of a molecular vibration to increase is to excite the bond by having it absorb light energy. For any given transition between two states the light energy (determined by the wavelength) must exactly equal the difference in the energy between the two states (usually ground state (E_0) and the first excited state (E_1)).

Difference in energy states = Energy of light absorbed

$$E_1 - E_0 = hc / \lambda \tag{1.36}$$

where h = Planks constant

c = speed of light

λ = the wavelength of light

The energy corresponding to these transitions between molecular vibrational states is generally 1-10 kilocalories/mole which corresponds to the infrared portion of the electromagnetic spectrum.

1.9.8.4 Sample preparation

Samples for FT-IR can be prepared in a number of ways. For liquid samples, the easiest is to place one drop of sample between two plates of sodium chloride (salt). Salt is transparent to infrared light. The drop forms a thin film between the plates. Solid samples can be milled with potassium bromide (KBr) to form a very fine powder. This powder is then compressed into a thin pellet which can be analyzed. KBr is also transparent in the IR. Alternatively, solid samples can be dissolved in a solvent such as methylene chloride, and the solution placed onto a single salt plate. The solvent is then evaporated off, leaving a thin film of the original material on the plate. This is called a cast film, and is frequently used for polymer identification. Solutions can also be analyzed in a liquid cell. This is a small container made from NaCl (or other IR-transparent material) which can be filled with liquid, such as the extract for EPA 418.1 analysis. This creates a longer path length for the sample, which leads to increased sensitivity. Sampling methods include making a mull of a powder with hydrocarbon oil or pyrolyzing insoluble polymers and using the distilled pyrolyzate to cast a film. Films can be placed in an Attenuated Total Reflectance (ATR) cell and for gases in gas cells.

1.10 Literature review of TiO_2

Martin et al. (1994) [95] investigated the effect of vanadium-doped (1 at.%) TiO_2 prepared by co-precipitation method on the crystallite and particle sizes, the crystal form, and surface structure (e.g., density of surfacial hydroxyl ions) were elucidated. These modifications of co-precipitation method was the important factors governing the differences in the photoactivities of doped and undoped-TiO_2. Vanadium dopant in TiO_2 is found to be present primarily as a solid solution.

Navío et al. (1996) [96] reported Fe (0.5-5%) doped TiO_2 were prepared by the wet impregnation method. Photocatalytic activity of iron doping TiO_2 was still lower than pure TiO_2 under UVA irradiation. No degradation was found under visible light irradiation because this method provides a better homogeneous distribution of iron into TiO_2 particle keeping practically uncharged the specific surface area of the catalyst.

Navío et al. again in 1999 [97] reported iron (0.5-5 wt.%) doped titanium dioxide semiconductor powders prepared by sol-gel method using $TiCl_4$ and Fe(III) acetylacetonate. The crystallite sizes of 5 wt.% Fe-doped TiO_2 smaller than the undoped sample. The 5 wt.% of Fe-doped TiO_2 sample showed X-ray peaks assigned to hematite and pseudobrookite (Fe_2TiO_5) phases. SEM micrographs of Fe-doped TiO_2 prepared by sol-gel showed an average size around 100-200 µm. EDX analysis of the 5 wt.% Fe-doped TiO_2 prepared by sol-gel showed iron uniformly distributed between particles and within one particle. The photocatalytic activity of EDTA oxidation was compared with impregnation of TiO_2 (Degussa P25) and found that the activity decreased under near UV irradiation.

Dhananjeyan et al. (2000) [98] the studied effect of dopants Fe^{3+} and calcination temperature on photodegradation rate. The Fe-doped TiO_2 catalyst was prepared by impregnation method using $Fe(NO_3)_3{\cdot}9H_2O$. The photocatalytic activity was investigated in uracil, thymine, 6-methyluracil and cytosine in an aqueous suspension was carried out. Fixed pH and initial concentration of the uracil, thymine, 6-methyluracil and cytosine and experiments were performed with varying amount of Fe-doped TiO_2. As amount of catalyst was increased, the number of photons absorbed corresponding to the number of catalyst particles. The density of particles of illumination also increases and the rate of photocatalytic activity was enhanced. The photocatalytic activity rate increased with decreasing the pH from 4.5 to 6.5 cause the enhanced of OH^- in TiO_2 surface (to give more h^+) showed the predominant role of the repelling electrostatic charge effect between the negatively charged pyrimidine based and the negatively charged surface of TiO_2. The rate of the photocatalytic process decreased with increasing of pretreatment temperature. It is clear that the photocatalysis in mainly mediated by $OH^{\cdot}$ produced via the step involving the attack of h^{+}_{vb} on surface bound water or OH^{-}. The density of surface hydroxyls varies with the annealing temperature. Effect of Fe^{3+} as a dopant, it is clear that the photooxidation rate increased with increasing in the level of Fe^{3+} doped onto TiO_2 up to approximately 0.75 at.% followed by a decrease in rate with further increase in Fe^{3+} level.

Anpo and Takeuchi (2001) [99] reported the influence of V, Mn, and Cr ions doped TiO_2 on photocatalytic reaction under visible light and solar light. UV-Vis absorption spectra showed the shifts in adsorption band toward visible light regions. Photocatalytic decomposition of NO_x could be operated effectively not only under UV light but also utilization of solar light and visible light irradiations.

Paola et al. (2002) [100] investigated the reaction of photooxidation with aliphatic and aromatic organic compounds having different acid strengths such as methanoic acid, ethanoic acid, benzoic acid and 4- nitrophenol. The polycrystalline TiO_2 powders were doped with various transition metal ions (Co, Cr, Cu, Fe, Mo, V and W). The transition metal ions doped TiO_2 were prepared by the impregnation method. The TiO_2 support was impregnated with aqueous solution of transition metal ions $Co(NO_3)_2{\cdot}H_2O$, $Cr(NO_3)_3{\cdot}9H_2O$, $Cu(NO_3)_2{\cdot}3H_2O$, $Fe(NO_3)_3{\cdot}9H_2O$, $(NH_4)_6Mo_7O_{24}{\cdot}4H_2O$, NH_4VO_3 and $(NH_4)_6W_{12}O_{39}{\cdot}xH_2O$. The doped TiO_2 were characterized by XRD, BET, PZC and testing photoactivity. The Co-doped TiO_2 powder showed more photoactive than the bare TiO_2 for methanoic acid degradation while the behavior of Cu-doped TiO_2 and Fe-doped TiO_2 was similar to bare TiO_2. The efficiency of W-doped TiO_2 was the measurement of the degradation rate of benzoic acid and 4- nitrophenol, while bare TiO_2 the most active powder for ethanoic acid.

Beydoun et al. (2002) [101] observed optimum Cu (II) concentration of 2 at.% enhanced photocatalytic degradation of sucrose. The overall lower oxidation rates observed at the low pH were believed to be due to factors such as the TiO_2 surface area being abundant of H^+ which interfered with the transfer of holes to the surface hydroxyl groups.

Li et al. (2002) [102] demonstrated the influence of the pH value upon the grain size. The concentration volume ratio of tetra-n-butyl titanate: deionized water were chosen as 1:2, 1:6, 1:12, 1:20, 1:50, and 1:100. The results showed that the different preparation condition such as concentration, pH value, calcination time, and calcination temperature had many effects upon the properties of TiO_2 nanopowder. The grain sizes were increased with the increasing calcination temperature and pH value. TEM result showed the particle size in the range of 6-36 nm at the calcination temperatures of 350, 500 and 600 °C.

Yamashita et al. (2003) [103] improved the electronic properties of the TiO_2 photocatalyst to realize the utilization of visible light. Preparation TiO_2 powder was prepared by sol-gel method from ethanolic solution of titanium tetraisopropoxide (TTIP) (got only anatase phase and crystal size 10.2 nm). Metal ion implanted TiO_2 photocatalysts were prepared for Fe-doped TiO_2 by the metal ion-implanted method. The effective photocatalytic activity were found to be in liquid phase for the degradation of 2-propanol under visible light. The Fe-doped TiO_2 could be absorbed in the range of visible region. Under the visible light irradiation of Fe ion implanted TiO_2 in a diluted aqueous solution of 2-propanol under O_2 atmosphere led to formation of acetone and CO_2. The Fe ions implanted TiO_2 photocatalysts exhibit a photocatalytic reactivity for the oxidative degradation of 2-propanol under visible light irradiation. The photocatalytic reactivity strongly depends on the amount of Fe ion.

Kang et al. (2003) [104] studied photocatalytic performance of Fe_xO_y/TiO_2 nanoparticles. The nanoparticles of Fe_xO_y/TiO_2 with high photocatalytic activities were obtained through hydrothermal treatment and impregnation method using titanium tetraisopropoxide (TTIP) and $Fe(NO_3)_3{\cdot}9H_2O$. The FeO_3 component on the external surface of the TiO_2 anatase structure was identified in the Fe-doped TiO_2 prepared by impregnation method. From XRD result, may be attributed to the fact that Fe component was well substituted into the Ti site in the case of impregnation method. The result of hydrothermal method was very useful in dispersing Fe component to Ti sites into TiO_2 anatase structure. The sizes of Fe_xO_y/TiO_2 synthesized by hydrothermal method and impregnation method were about 50 nm and 100 nm respectively. This study selected $CHCl_3$ to determine the photocatalytic performance of Fe_xO_y/TiO_2 under UV light. In this case of Fe_xO_y/TiO_2, the final conversion of Fe-incorporated TiO_2 was almost the same as that of pure TiO_2. It showed that $CHCl_3$ concentration of 100 ppm was enhanced by up to 10 wt.% of Fe concentration but decreased with an increase in the Fe component. The conversion of $CHCl_3$ was slightly higher on Fe_xO_y/TiO_2 synthesized through hydrothermal treatment than Fe loading TiO_2 particle prepared through the impregnation method.

Park et al. (2004) [105] studied chemical band structure of V-doped TiO_2 nanopowder synthesized by aerosol-assisted chemical vapor synthesis. The average diameter of TiO_2 nanopowder was about 7 nm and 200-240 m^2/g of specific surface area. Phase transition from anatase to rutile was found at the temperature of 600 °C. The particles size increased with increasing amount of vanadium contents. Titanium dioxide nanopowders showed the red shift behavior as well as a large visible absorption in UV-Vis spectra due to the formation of many bridging Ti-O-V bonds within the fully solid solution of $Ti_{1-x}V_xO_2$.

Su et al. (2004) [106] studied the sol–gel preparation and photocatalysis of titanium dioxide. Titanium dioxide was prepared by the hydrolysis and condensation of titanium (IV) n-butoxide in iso-propyl alcohol. The XRD peaks showed rutile phase became the major constituent of TiO_2 when increasing calcination temperature to 700 °C. The XRD data showed the crystal size of TiO_2 in the range of 4-35 nm and BET surface area recorded a significant decrease from 122 to 11.5 m^2g^{-1}. The photocatalytic activity was tested with salicylic acid. The photodegradative reaction of salicylic acid may be followed either fast or slow reaction channels, possibly corresponding to the anatase or rutile reaction sites on TiO_2 surface.

Wu et al. (2004) [107] reported the amount of V-doped TiO_2 were synthesized by two modified sol-gel method and studied photodegradation rates of crystal violet (CV) and methylene blue (MB). The first method, vanadyl acetylacetonate was dissolved in the n-butanol solution. Acetic acid was mixed in titanium butoxide in the molar ratio of titanium butoxide, acetic acid, n-butanol of 1:4:4. The hydrolysis process was completed after 24h and dried at 150 °C. The powder was calcined at 400 °C for 30 min (code V/TiO_2-NE). The second method, vanadium chloride was dissolved in ethanol and then mixed with titanium butoxide. The mixed solution was performed slowly drop by drop adding in a 0.1 M HCl solution and then quickly hydrolyzed with a due large amount of water. The solution was kept cooled at near 0 °C and then dried the solution at 100 °C. The powder was calcined at 400 °C for 30 min (code V/TiO_2). The powder was characterized by UV-Vis spectroscopy, XAS, TEM and XRD. The catalysts were stable in anatase phase at up to 700 °C and no characteristic peak of V oxide (V_2O_5 and V_2O_4). The crystallite sizes measured from peak broadening of XRD and the observation from TEM micrograph. The crystallite size increased with increasing vanadium. The N_2 adsorption was employed to study the specific surface area to V/TiO_2. The specific surface area of V/TiO_2-C and V/TiO_2-NE was found to be >100 m^2/g and 37-47 m^2/g respectively. The pore size of V/TiO_2-C and V/TiO_2-NE were found to be 6-8 nm and 20 nm respectively. The photodegradation of V/TiO_2 was tested with CV and MB. The V^{4+} is possible in octahedral lattice of TiO_2 but V^{5+} may be V_2O_5 within crystalline of TiO_2. Photodegradation rates of CV and MB with initial concentration 1.3×10^{-5} and 2.8×10^{-5} M respectively, under visible light. The photocatalytic activity was degraded MB faster than CV. The V-doped TiO_2 prepared by sol-gel successful shift to visible light and V-doped TiO_2 was higher than pure TiO_2 under visible light.

Zhu et al. (2005) [108] observed Fe-doped TiO_2 prepared by sol-gel method. Iron ions were uniformly distributed in the interstices of TiO_2 crystals to form solid solution. The photocatalytic activity was evaluated by the degradation of yellow XRG dye under UV and visible irradiation. Their photo-activity could not be enhanced so obviously under UV or visible irradiation. It was possible that Fe^{3+} was doped uniformly from the exterior to the interior by sol-gel method and the existence of solubility limit for Fe ions in TiO_2 led to the formation of α-Fe_2O_3 at higher concentrations.

Zhou et al. (2005) [109] investigated the effect of the amount of iron in doped mesoporous titanium dioxide nanocrystalline photocatalyst prepared by the sol-gel method on photocatalytic oxidation of acetone. The iron oxide or Fe_xTiO_y phases were not found in the XRD pattern because a small of amount of Fe-doping, hence it could not detect by XRD. The crystallite size of XRD was calculated from Scherrer equation was decreased when increasing the amount of iron. The surface area decreased when the amount of Fe increased. XPS studies showed that all Fe-doped mesoporous TiO_2 powders contained Fe^{3+} (35.0%) and Fe^{2+} (65.0%) ions. The photocatalytic activity was evaluated by the photocatalytic oxidation of acetone in air. It was found that a small amount of Fe dopant in mesoporous TiO_2 powder could obviously enhanced the photocatalytic activity, and when the atomic ratio of Fe/Ti was in the range of 0.05-0.25%, the photocatalytic activity of the samples was higher than Degussa P25 and undoped mesoporous TiO_2 powders.

Teoh et al. (2007) [44] reported Fe-doped TiO_2 synthesized by Flame Spray Pyrolysis (FSP) and proposed that Fe(III) formed a complex with oxalate which was easily photolyzed to produce CO_2 and Fe(II) ions under visible light irradiation. The photocatalytic activity of the FSP Fe-doped TiO_2 could be re-generated by the oxidation of adsorbed Fe(II) to Fe(III) under visible light irradiation.

1.11 Research objectives

1. To develop the reproducible preparation methods based on the modified sol-gel method for preparing pure and V, Fe, Cu-doped TiO_2 and the impregnation method for preparing Fe-doped TiO_2
2. To characterize the physical and chemical properties of pure and V, Fe, Cu-doped TiO_2
3. To study the photocatalytic activity on sucrose, phenol, oxalic acid, formic acid, methanol, and malonic acid which were used as the model representing for organic compounds
4. To identify the optimum conditions suitable for preparation of pure and V, Fe, Cu-doped TiO_2 using the developed by the modified sol-gel method
5. To identify the best catalyst for photocatalytic activity